Final Scientific Report

on

NASA GRANT NSG-1351

Elastic-Plastic Finite Element Analyses of Fatigue Crack Growth in Mode I and Mode II Conditions

Submitted by

Michihiko Nakagaki

and

Satya N. Atluri

School of Engineering Science and Mechanics
Georgia Institute of Technology
Atlanta, Georgia 30332

November 1978

Final Scientific Report

on

NASA GRANT NSG-1351

Elastic-Plastic Finite Element Analyses of Fatigue Crack Growth in Mode I and Mode II Conditions

Submitted by

Michihiko Nakagaki

and

Satya N. Atluri

School of Engineering Science and Mechanics
Georgia Institute of Technology
Atlanta, Georgia 30332

November 1978

Foreward

This report is based on research performed under NASA Grant NSG-1351, NASA Langley Research Center, at the School of Engineering Science and Mechanics, Georgia Institute of Technology. The technical monitor for the grant was Dr. J. C. Newman, Jr. of NASA Langley Research Center. The Principal Investigator for the grant at Georgia Tech was Professor Satya N. Atluri

Contents

1. Introduction

The phenomenon of fatigue-crack-closure, first discovered experimentally by Elber [1,2], continues to be a subject of several recent experimental and analytical studies; see, for instance, Refs. [3,4]. Elber has also originally postulated that the crack-closure phenomenon is caused by residual plastic deformations remaining in the wake of the advancing crack-tip.

Analytical models that lend theoretical support to the existence of the crack-closure phenomenon in fatigue crack growth, and provide some rationality for the adoption of an effective stress-intensity range, based on closure effects, for the correlation of fatigue crack growth rate, have also been proposed by Budiansky and Hutchinson [5].

As for a more general analysis of extending cracks under general block cyclic loading, to obtain crack-closure stresses, crack-opening stresses, details of crack-surface displacement, and residual stresses in the crack-tip region, etc., elastic-plastic finite element analyses were first performed by Newman and his colleagues [6,7,8]. Apart from these analyses, the authors are aware of similar attempts only by Ohji and his co-workers [9,10]. The studies in [6-10] considered the Mode I case only. Also, since the crack growth was simulated in [6-10] by shifting a finite element node (the current crack-tip) to an immediately adjacent node, and since constant strain triangle type finite elements were used to model the cracked structure, a very fine finite element mesh (with the smallest element often being of the order of 10^{-3} times the crack length) is necessary in the modeling procedures of [6-10]. This can be very expensive especially when cyclic loads of arbitrary spectrum are considered.

One of the objectives of the present report is to present an alternate cost-efficient and accurate elastic-plastic finite element procedure to

analyse fatigue crack closure and its effects under general spectrum loading. Both Modes I and II type cycling loadings are considered. Also presented in this report are the results of an investigation, using the newly developed procedure, of various factors that cause crack growth acceleration or retardation and delay effects under high-to-low, low-to-high, single overload, and constant amplitude type cyclic loading in a Mode I situation. Further, the results of an investigation of a center-cracked panel under external pure shear (Mode II) cyclic loading, of constant amplitude, are reported.

2. A Synopsis of the Present Analysis Procedure

Before embarking on a presentation of the mathematical details, the salient features of the presently reported analysis procedure are given below:

(i) The present elastic-plastic finite element procedure accounts for arbitrary strain-hardening material behaviour; the mathematical description of incremental elastic-plastic flow consists of Huber-Mises-Hencky yield criterion, and a Prager-Ziegler type kinematic hardening rule which best models the Bauschinger effects.

(ii) The well-known Hutchinson-Rice-Rosengren [11,12] type strain and stress singularities, for strain-hardening materials, are embedded in specially developed elements near the crack-tip. This eliminates the need for a very fine mesh near the tip. For instance, the crack-tip elements in the present procedure are of the order 10^{-1} of the crack length, as compared to constant strain triangles of the order of 10^{-3} to 10^{-4} times the crack length generally used in the procedures of [6-10]. A hybrid displacement finite element method [13,14] is used in developing these special elements.

(iii) The above special hybrid elements are of circular-sector shape, centered at the crack-tip; thus enabling one to model crack growth in any arbitrary direction, from the crack-axis, under general mixed mode cyclic loading.

(iv) In the present procedure, crack-growth is simulated by: (a) translation of the core of circular-sector elements, with embedded H-R-R singularities, by an arbitrary amount in the desired direction, (b) reinterpolation of requisite data in the new finite element mesh, and (c) proportional relaxation of tractions in order to create a new crack surface.

(v) In order to most accurately determine the crack-opening stress σ_{op} and crack-closure stress $\sigma_{c\ell}$, the displacements at nodes on the crack-axis before closure (and after opening), as well as the restraining force at the corresponding nodes after crack-closure (and before opening) are extrapolated against the load level. In all the cases studied, these two sets of extrapolated values for σ_{op} and $\sigma_{c\ell}$ were found to correlate excellently.

(vi) A static-condensation procedure is employed wherein the plastic portion of the structure is isolated from the elastic; the stiffness of only the former part keeps changing whereas that of the latter remains fixed. This results in a considerable saving of the computational time. This and the invocation of the appropriate anti-symmetric and symmetric conditions for modes II and I problems, along with the use of special elements of a large size as described in (ii) above, reduce the analysis procedure to be feasible as a routine tool in design, if necessary.

(vii) A study is made to arrive at a criterion for the stress level σ_{ex}, at which fatigue crack growth occurs. In prior literature, this crack extension stress level was chosen arbitrarily. For instance, in [6-8] the crack is extended at the maximum applied stress in each cycle in a spectrum

loading, whereas in [9,10] the crack was extended at the applied stress level at which the restraining nodal force at the new crack-tip becomes zero. In the present study, for instance in a constant-smplitude (zero to tension) cyclic loading, it was found that σ_{op} and $\sigma_{c\ell}$ were very sensitive to the chosen σ_{ex}. In the present work, a criterion, $\sigma_{ex} = p(\sigma_{max} - \sigma_{op}) + \sigma_{op}$ where p is a constant of proportionality, is postulated; and p is obtained by calibration such that the calculated σ_{op} correlated with that observed in experimental studies such as in [1,2,3]. However, it is not claimed that this is a general criterion; it is recognized that it is dependent on material properties, and to an extent on the analysis procedure itself. The mathematical details of the above features are discussed in the following.

3. Elastic-Plastic, Embedded Singularity, Incremental Finite Element Method, Based on Hybrid Displacement Model, For Analysing Cracked Structures

To start with, we use circular-sector shaped "singularity" elements near the crack-tip, as shown in Fig. 1. In these singularity elements, a displacement field which corresponds to strain and stress singularities, for strain-hardening elastoplastic materials, of the well-known Hutchinson-Rice-Rosengren [11,12] type, is assumed. The above singularity elements are surrounded by "regular" eight-node isoparametric quadrilateral elements, as shown in Fig. 2. Compatibility of displacements and continuity of tractions between these "regular" and "singular" elements is enforced through a Lagrangean Multiplier technique as shown below.

The incremental analysis of the present elasto-plastic problem is based on a continuously updated Lagrangean (coordinate-system) formulation. In the following, for simplicity, we consider the formulation in the context of a general three-dimensional problem and present only the essential mathematical details. We consider a fixed cartesian coordinate system, and

consider C_N to be the 'state' (viz. deformation, strain, and stress) of the structure before the addition of the Nth load-increment. Let x_i be the material coordinates of a point in the initial, undeformed and unstressed configuration, C_1. Let u_i^N be the displacement, measured in the fixed cartesian system, of a point in C_1 to the deformed state C_N. The new coordinates of the material point in C_N then become $X_i^N = x_i + u_i^N$. Let the (symmetric) Eulerean (true) stress tensor in C_N be τ_{ij}^N, measured per unit area in C_N and in the metric of the fixed cartesian system. Let the body forces/unit volume in C_N be F_i^N and prescribed surface traction/unit area in C_N be $\bar{T}_i^N$.

Let additional body forces ΔF_i (per unit C_N volume) and additional surface tractions $\Delta\bar{T}_i$ (per unit C_N area) be applied during the movement of the structure from C_N to C_{N+1}. Let additional cartesian displacements of the material point in moving from C_N to C_{N+1} be Δu_i; thus $X_i^{N+1} = X_i^N + \Delta u_i$ are the new coordinates of a material point in C_{N+1}. The incremental Green strain $\Delta^* g_{ij}$ from C_N to C_{N+1}, with reference to the metric in C_N can then be written as,

$$\Delta^* g_{ij} = \frac{1}{2}\left[\frac{\partial \Delta u_i}{\Delta X_j^N} + \frac{\partial \Delta u_j}{\partial X_i^N}\right] + \frac{1}{2}\left[\frac{\partial \Delta u_K}{\partial X_i^N}\frac{\partial \Delta u_K}{\Delta X_j^N}\right] \equiv \Delta e_{ij}^* + \Delta\eta_{ij}^* \qquad (3.1)$$

During the motion from C_N to C_{N+1}, the state C_N is treated as one with "initial stresses". The new stresses in C_{N+1} due to the additional incremental loading, will be represented by the symmetric second Piola-Kirchhoff stress tensor $S_{ij(N)}^{N+1}$, which is measured per unit area in C_N.

$$S_{ij(N)}^{N+1} = \tau_{ij}^N + \Delta^* S_{ij} \qquad (3.2)$$

Assuming the material has yielded, the relation between the incremental

stress[+] ($\Delta^* S_{ij}$) and the incremental strain $\Delta^* g_{ij}$ will be written as

$$\Delta^* S_{ij} = E^t_{ijk\ell} \, (\tau^N_{ij}) \, \Delta^* g_{k\ell} \tag{3.3}$$

where $E^t_{ijk\ell}$ is the current constitutive property, as modified by plasticity, and is a function of current true stress, τ^N_{ij}. Such a constitutive relation, based on the well-known Huber-Mises-Hencky yield criteria, Drucker's normality condition, and a Prager-Ziegler type kinematic hardening law has been derived for the present plane stress conditions, following the procedure described in Ref. 13.

Based on this, it can be shown that the variational principle governing the equilibrium of state C_{N+1} is $\delta\Delta\pi_{HD} = 0$ where,

$$\Delta\pi_{HD}(\Delta u_i, \Delta v_i, T_{Li}) = \sum_{m=1}^{P} \left\{ \int_{\Omega_m} \left[\left(\tau^N_{ij} + \frac{1}{2} \Delta^* S_{ij} \right) \Delta^* e_{ij} + \frac{1}{2} \tau^N_{ij} \Delta u_{k,i} \Delta u_{k,j} \right.\right.$$

$$\left.\left. - (F^N_i + \Delta F_i)\Delta u_i \right] da - \int_{\partial\Omega_m} T_{Li}(\Delta u_i - \Delta v_i) ds - \int_{S_{\sigma_m}} (\bar{T}_i + \Delta\bar{T}_i)\Delta v_i ds \right\} \tag{3.4}$$

where

Ω_m = domain of the m^{th} finite element,

$\partial\Omega_m$ = boundary of the m^{th} finite element,

S_{σ_m} = a portion of $\partial\Omega_m$ where tractions are prescribed,

τ^N_{ij} = true (Euler) stress in C_N, measured/unit area in C_N and in the fixed cartesian metric,

$F^N_i, \bar{T}_i$ = body force and surface traction, per unit volume and per unit area, respectively, in C_N,

---

[+] The Stress-increment $\Delta^* S_{ij}$ is commonly referred to as the Truesdell stress-increment. This stress-rate is objective [15,16].

$$\Delta e^*_{ij} = \frac{1}{2}\left[\frac{\partial \Delta u_i}{\partial X^N_j} + \frac{\partial \Delta u_j}{\partial X^N_i}\right]; \quad \Delta S^*_{ij} = E^t_{ijk\ell}(\tau^N_{ij})\ \Delta^* e_{k\ell} \tag{3.5}$$

Δu_i = arbitrarily assumed displacements, in each element, that need not satisfy interelement compatibility a priori. In elements surrounding the crack-tip, displacements corresponding to the Hutchinson-Rice-Rosengren singularities, for hardening materials, are included.

Δv_i = independently assumed displacements at the element boundary, $\partial\Omega_m$, which inherently satisfy inter-element compatibility criteria,

T_{Li} = Lagrange Multiplier to enforce the compatibility condition, $\Delta u_i = \Delta v_i$ at $\partial\Omega_m$, and

$\Delta F_i, \Delta\bar{T}_i$ = prescribed increments of body forces and surface tractions, respectively, measured unit volume and unit area, respectively in C_N.

The Euler equations corresponding to $\delta\Delta\pi\ (\delta\Delta u_i,\ \delta\Delta v_i,\ \delta T_{Li}) = 0$ lead to,

$$\Delta^* S_{kj,j} + \left(\tau^N_{ij}\Delta u_{k,j}\right)_{,i} + \Delta\bar{F}_k + \left\{\tau^N_{kj,j} + \bar{F}_k\right\} = 0 \tag{3.6}$$

$$\left(\tau^N_{kj} + \Delta^* S_{kj}\right)n_j + \tau^N_{ij}\Delta u_{k,j}n_i = T_{Lk} \text{ at } \partial\Omega_m \tag{3.7}$$

$$\bar{T}_i + \Delta\bar{T}_i = T_{Li} \text{ at } S_{\sigma_m} \tag{3.8}$$

and

$$\Delta u_i = \Delta v_i \text{ at } \partial\Omega_m \tag{3.9}$$

In the above, a comma followed by an index such as i, is meant to designate a partial differentiation with respect to the cartesian coordinate, X_i^N. Eq. (3.6) refers to the equilibrium of the total second Piola-Kirchhoff stress $S_{ij(N)}^{N+1}$ in C_{N+1}. If state C_N was in true equilibrium, the last two bracketed terms in Eq. (3.6) would be equal to zero. However, because of the inherent numerical errors in the incremental solution process, the state C_N may not be truly equilibrated. Thus, retaining the last two terms in Eq. (3.6) leads to an "equilibrium-check" iteration process, similar to the one described in detail by Hofmeister, et al [17]. Eq. (3.7) states that the tractions derived from the assumed incremental interior displacements match the independently assumed boundary tractions, T_{Li}. Finally, Eq. (3.9) is the statement of inter-element displacement compatibility that is <u>enforced</u> in the present method, by means of Lagrange Multipliers, T_{Li}.

Because of the advantages of the above described hybrid-displacement model, and the convenience of the conventional finite-element displacement model, a combination of both the methods is used in the present formulation. Thus one can visualize the domain of the cracked structure to be divided into two regions, (a) a small region near the crack-tip where the singular, near field solution is predominant, and (b) a region away from the crack-tip where the effect of the singularity is not dominant. In the present calculations, a hybrid-displacement model is used to derive the stiffness properties of the near-tip sector elements, and the conventional displacement model is used to derive the stiffness properties of the far-field, eight-node isoparametric elements.

Consider first the development of the properties of the near-tip, circular-sector shaped "singular" elements, wherein, the three independent

variables Δu_i, Δv_i, and T_{Li} are assumed as follows*:

$$\underset{\sim}{\Delta u}_i = \underset{\approx}{A}\,\underset{\sim}{\beta},\quad \underset{\sim}{\Delta v}_i = \underset{\approx}{L}\,\underset{\sim}{\Delta q};\quad \underset{\sim}{T}_{Li} = \underset{\approx}{R}\,\underset{\sim}{\alpha} \tag{3.10}$$

where $\underset{\sim}{\beta}$, and $\underset{\sim}{\alpha}$ are unknown independent parameters, and $\underset{\sim}{\Delta q}$ are increments of nodal displacements during the generic load step, $C_N \rightarrow C_{N+1}$. The functions $\underset{\approx}{A}$ and $\underset{\approx}{R}$ are arbitrary. However, $\underset{\approx}{L}$ are functions ar the boundary of the circular-sector element such that they uniquely interpolate for Δv at the boundary in terms of the relevant Δq at the boundary, and in addition, ensure displacement-compatibility with the surrounding 8-noded isoparametric quadrilateral elements (Fig. 2).

For far-field regular elements, as mentioned earlier, the conventional compatible displacement finite element model is used. The incremental energy functional corresponding to this model can be expressed as,

$$\begin{aligned}\Delta\pi_{CD}(\Delta u_i) = \sum_{m=p+1}^{m} \Big\{ \int_{\Omega_m} \Big(&\frac{1}{2} E^t_{ijkl} \Delta\varepsilon_{kl} \Delta\varepsilon_{ij} + \frac{1}{2} \tau^N_{ij} \Delta u_{k,i} \Delta u_{k,j} \\ &- \Delta\bar{F}_i \Delta u_i \Big) da - \int_{S_{\sigma_m}} \Delta\bar{T}_i \Delta u_i \, ds + \int_{\Omega_m} (\tau^N_{ij} \Delta u_{i,j} - \bar{F}^N_i \Delta u_i) da \\ &- \int_{S_{\sigma_m}} \bar{T}^N_i \Delta u_i \, ds \Big\}\end{aligned} \tag{3.11}$$

The finite-element approximations for a far-field regular element are considered as,

$$\underset{\sim}{\Delta u} = \underset{\approx}{D}\,\underset{\sim}{\Delta q} \tag{3.12}$$

*The usual notation, ($\sim$) under a symbol, is used to denote a column vector, and ($\approx$) under a symbol is used to denote a matrix.

from which the strains and deformation gradients are derived as,

$$\underset{\sim}{\Delta\varepsilon} = \underset{\approx}{B}\ \underset{\sim}{\Delta q}\ \underset{\sim k,i}{\Delta u} = \underset{\sim k}{W}\ \underset{\sim}{\beta} \tag{3.13}$$

For purposes of convenience of notations we consider that, out of a total of M finite elements, m = 1, p are the so-called singular elements and m = p+1 ...M are the far-field regular elements.

The assumptions for the field variables as in Eq. (3.10) for elements m = 1,...p are substituted into Eq. (3.4) and the first variation of π_{HD} with respect to the parameters α and β is set to zero, to obtain, for elements m = 1, p, that

$$\underset{\sim}{\alpha} = \underset{\approx}{P}^{-T}(\underset{\approx}{H} + \underset{\approx g}{C})\underset{\approx}{P}^{-1}\ \underset{\approx}{G}\ \underset{\sim}{\Delta q} + \underset{\approx}{P}^{-T}\ \underset{\sim e}{C} - \underset{\approx}{P}^{-T}\underset{\sim 4}{F} \tag{3.14}$$

$$\underset{\sim}{\beta} = \underset{\approx}{P}^{-1}\underset{\approx}{G}\ \underset{\sim}{\Delta q} \tag{3.15}$$

where,

$$\underset{\sim}{\Delta\varepsilon} = \underset{\approx}{W}\ \underset{\sim}{\beta},\ \underset{\sim k,i}{\Delta u} = \underset{\sim k}{W}\ \underset{\sim}{\beta} \tag{3.16}$$

$$\underset{\approx}{H} = \int_{\Omega_m} \underset{\approx}{W}^T \underset{\approx}{E}\ \underset{\approx}{W} dA \tag{3.17}$$

$$\underset{\approx}{P} = \int_{\partial\Omega_m} \underset{\approx}{R}^T \underset{\approx}{A}\ ds \tag{3.18}$$

$$\underset{\approx}{G} = \int_{\partial\Omega_m} \underset{\approx}{R}^T \underset{\approx}{L}\ ds \tag{3.19}$$

$$\underset{\approx g}{C} = \int_{\Omega_m} \left(\underset{\sim 1}{W}^T\ \underset{\approx ij}{\tau^N}\ \underset{\sim 1}{W} + \underset{\sim 2}{W}^T\ \underset{\approx ij}{\tau^N}\ \underset{\sim 2}{W}\right) dA \tag{3.20}$$

and

$$\underset{\sim e}{C} = \int_{\Omega_m} \underset{\approx}{W}^T\ \underset{\approx}{\tau^N}\ dA \tag{3.21}$$

Substituting for $\underset{\sim}{\alpha}$ and $\underset{\sim}{\beta}$ from Eqs. (3.14 and 15) into Eq. (3.4), one can express $\Delta\pi_{HD}$ in terms of $\Delta\underset{\sim}{q}$ only, as,

$$\Delta\pi_{HD} = \sum_{m=1}^{p} \frac{1}{2} \Delta\underset{\sim}{q}^T (\underset{\approx}{K} + \underset{\approx}{K}_g) \Delta\underset{\sim}{q} - \Delta\underset{\sim}{q}^T \Delta\underset{\sim}{Q} - \Delta\underset{\sim}{q}^T \Delta\underset{\sim}{Q}_C \tag{3.22}$$

where,

$$\underset{\approx}{K} = (\underset{\approx}{P}^{-1}\underset{\approx}{G})^T \underset{\approx}{H} (\underset{\approx}{P}^{-1}\underset{\approx}{G}) \tag{3.23}$$

$$\underset{\approx}{K}_g = (\underset{\approx}{P}^{-1}\underset{\approx}{G})^T \underset{\approx}{C}_g (\underset{\approx}{P}^{-1}\underset{\approx}{G}) \tag{3.24}$$

$$\Delta\underset{\sim}{Q} = \underset{\sim}{F}_2 = \int_{S_{\sigma_m}} \underset{\approx}{L}^T \Delta\bar{\underset{\sim}{T}} \, ds \tag{3.25}$$

and

$$\Delta\underset{\sim}{Q}_c = (\underset{\approx}{P}^{-1}\underset{\approx}{G})^T (\underset{\sim}{F}_4 - \underset{\sim}{C}_e) \tag{3.26}$$

Likewise the assumptions for the field variable in Eq. (3.12) for elements m = p + 1 --M are substituted into Eq. (3.11) to obtain $\Delta\pi_{cD}$, for elements m = p + 1---M, as,

$$\Delta\pi_{cD} = \sum_{p+1}^{M} \frac{1}{2} \Delta\underset{\sim}{q}^T (\underset{\approx}{K}^R + \underset{\approx}{K}_g^R) \Delta\underset{\sim}{q} - \Delta\underset{\sim}{q}^T \underset{\sim}{F}_2^R - \Delta\underset{\sim}{q}^T (\underset{\sim}{F}_4^R + \underset{\sim}{C}_e^R) \tag{3.27}$$

where,

$$\underset{\approx}{K}^R = \int_{\Omega_m} \underset{\approx}{B}^T \underset{\approx}{E}^t \underset{\approx}{B} \, dA, \tag{3.28}$$

$$\underset{\approx}{K}_g^R = \int_{\Omega_m} (\underset{\approx}{W}_1^T \underset{\approx}{\tau}_{ij}^N \underset{\approx}{W}_1 + \underset{\approx}{W}_2^T \underset{\approx}{\tau}_{ij}^N \underset{\approx}{W}_2) \, dA \tag{3.29}$$

$$\underset{\sim}{C}_e^R = \int_{\Omega_m} \underset{\approx}{B}^T \underset{\sim}{\tau}^N \, dA \tag{3.30}$$

$$\underset{\sim}{F}_2^R = \int_{s_{\sigma_m}} \underset{\approx}{D}^T \, \Delta\bar{\underset{\sim}{T}} \, ds \tag{3.31}$$

and

$$F_4^R = \int_{s_{\sigma_m}} \underset{\approx}{D}^T \, \bar{\underset{\sim}{T}}^N \, ds \tag{3.32}$$

Combining Eqs. (3.22) and (3.27), the total energy functional for the system, $\Delta\pi$, can be written as,

$$\Delta\pi = \sum_{m=1}^{p} \left[\frac{1}{2} \, \Delta\underset{\sim}{q}^T (\underset{\approx}{K} + \underset{\approx}{K}_g) \, \Delta\underset{\sim}{q} - \Delta\underset{\sim}{q}^T \, \Delta\underset{\sim}{Q} - \Delta\underset{\sim}{q}^T \Delta\underset{\sim}{Q}_c \right]$$

$$+ \sum_{m=p+1}^{M} \left[\frac{1}{2} \, \Delta\underset{\sim}{q}^T (\underset{\approx}{K}^R + \underset{\approx}{K}_g^R) \, \Delta\underset{\sim}{q} - \Delta\underset{\sim}{q}^T \, \Delta\underset{\sim}{Q}^R - \Delta\underset{\sim}{q}^T \Delta\underset{\sim}{Q}_c^R \right] \tag{3.33}$$

where,

$$\Delta\underset{\sim}{Q}^R = \underset{\sim}{F}_2^R; \text{ and } \Delta\underset{\sim}{Q}_c^R = \underset{\sim}{F}_4^R + \underset{\sim}{C}_e^R. \tag{3.34}$$

By expressing the element incremental nodal displacements $\Delta\underset{\sim}{q}$ in terms of independent generalized global displacements Δq^*, and using the condition of stationarity of $\Delta\pi$ with repect to Δq^*, one obtains the final expression,

$$\left[K(q_N, P_N) \right] \left\{ \Delta q^* \right\}_N^{N+1} = \left\{ \Delta Q(q_N, P_N) \right\} + \left\{ \Delta Q_{ec} \right\} \tag{3.35}$$

where

$\{q\}_N$ = generalized nodal displacements in state C_N (with loads P_N)

$[K(q_N, P_N)]$ = the tangent stiffness matrix at state C_N which includes the effects of initial stresses, displacements, and the influence of plastic yielding at state C_N,

$\{\Delta q^*\}_N^{N+1}$ = incremental displacements of the structure from C_N to C_{N+1},

$\{\Delta Q(q_N, P_N)\}$ = incremental loads, and

$\{\Delta Q_{ec}\}$ = residual nodal forces to check the equilibrium of state C_N.

The solution of Eq. (3.35) with a Newton-Raphson type equilibrium correction iteration, is essentially similar to that presented by Hofmeister et al [17], and further details are omitted. Finally, we note that in order to carry our the incremental solution from C_{N+1} to C_{N+2}, the second Piola-Kirchhoff stresses $S^{N+1}_{ij(N)}$ are converted to Euler (true) stresses in C_{N+1}, using the relation,

$$\tau^{N+1}_{ij} = \frac{1}{\text{Det}\left[\frac{\partial X^{N+1}_i}{\partial X^N_j}\right]} \frac{\partial X^{N+1}_i}{\partial X^N_K} \frac{\partial X^{N+1}_j}{\partial X^N_\ell} S^{N+1}_{k\ell(N)} \tag{3.36}$$

4. Details of Finite Element Field Assumptions

4.1 Circular-Sector Shaped Singular Elements

The dominant singularities in strains and stresses at the tip of a crack in a monotonically loaded two dimensional body of a nonlinear material obeying a power-hardening law of plasticity were analysed by Hutchinson [11] and Rice and Rosegren [12]. (Hereafter these are referred to as the H.R.R singularities.) Their analyses were based on a deformation theory of plasticity; however, to an approximation, these are considered to be valid, in the present work, when a flow theory of plasticity is used. Further, the analysis in [11,12] are valid only for stationary cracks. However, the nature of singularities at the tip of a moving crack in an elastic-plastic solid is still largely uncertain. The existing attempts in the literature to obtain analytical solutions to the problem of a "steadily" moving crack-tip in perfectly plastic materials, by Chitaley and McClintock [18] and Rice [19],

show a logarithmic strain-singularity at the crack-tip. However, one of these solutions [18] has been recently argued by Broberg [20] to be in error. Due to these reasons, and for lack of criteria to define "steady" state conditions, a priori, the H-R-R singularities [11,12] are allowed, in the present analysis, to be present at the crack-tip which grows under fatigue loading. This may, however, be viewed as an approximation in the general context of the finite element method, in the sense that the hypothetical exact solution is approximated by a set of assumed basis functions. It is also noted that in spite of this approximation, the crack surface deformation profiles, after fatigue carck extension, to be discussed later, do suggest a possible change in the nature and order of strain singularities near the growing crack-tip. Finally, we note that if the nature singularities near the advancing crack-tip both in the "transitory" as well as "steady state" conditions is clarified analytically, it is, in principle, possible to affect the appropriate changes in the present finite element modeling.

The H-R-R solution for the dominant solution near the crack-tip for stresses, strains, and displacements, respectively, can be expressed as:

$$\sigma_{ij} \sim k_\sigma \, r^{-1/n+1} \bar{\sigma}_{ij}(\varphi) \tag{4.1}$$

$$\epsilon_{ij} \sim k_\epsilon \, r^{-n/n+1} \bar{\epsilon}_{ij}(\varphi) \tag{4.2}$$

and

$$u_i \sim k_\epsilon \, r^{1/n+1} \bar{u}_i(\varphi) \tag{4.3}$$

where (r and φ) are polar coordinates centered at the crack-tip; n is the power hardening exponent in the Ramberg-Osgood relation between the equivalent stress $\bar{\sigma}$ and equivalent plastic strain $\bar{\epsilon}_p$, viz., $\bar{\epsilon}_p \sim \bar{\sigma}$; k_σ and k_ϵ are constants; and $\bar{\sigma}^n_{ij}(\varphi)$, $\bar{\epsilon}_{ij}(\varphi)$ and $\bar{u}_i(\varphi)$ are functions of the angular coordinate φ (see Fig. 1).

The above dominant singularities are embedded in the sector shaped "singularity" elements surrounding the crack-tip. More over these singular functions are augmented, in the singularity elements, by a large number of arbitrary polynomial functions for displacements and strains. Due to this reason, the singularity elements in the present analysis can be fairly large; in the numerical examples presented later, these elements are, in general, chosen to be about 10^{-1} times the crack length.

4.1.1 Displacements in the Interior of Singular Element

Based on the above reasoning, the incremental displacements in the singularity elements are assumed as:

$$\Delta u_r = \beta_1 r + 2\beta_2 r\theta + \beta_3 r\theta^2 + \beta_5 r^2 + \beta_6 r^2\theta + \beta_{10}\cos\varphi\, r^{1/n+1} + \beta_{11}\cos\varphi\, r^{1/n+1}\theta + \beta_{12}\cos\varphi\, r^{1/n+1}\theta^2 + \beta_{13}\sin\varphi\, r^{1/n+1} + \beta_{14}\sin\varphi\, r^{1/n+1}\theta + \beta_{15}\sin\varphi\, r^{1/n+1}\theta^2 \tag{4.4}$$

$$\Delta u_\theta = \beta_2 r + \beta_4 r\theta + \beta_7 r\theta^2 + \beta_8 r^2 + \beta_9 r^2\theta - \beta_{10}\sin\varphi\, r^{1/n+1} - \beta_{11}\sin\varphi\, r^{1/n+1}\theta - \beta_{12}\sin\varphi\, r^{1/n+1}\theta^2 + \beta_{13}\cos\varphi\, r^{1/n+1} + \beta_{14}\cos\varphi\, r^{1/n+1}\theta + \beta_{15}\cos\varphi\, r^{1/n+1}\theta^2. \tag{4.5}$$

where β's are undetermined parameters, φ is the global angular coordinate; and θ is the angle measured from the symmetric axis of the sector element, as shown in Fig. 1. The above are augmented by the three rigid body modes for the element. Thus, using the matrix notation we write,

$$\underset{\sim}{\Delta u} = \underset{\approx}{A}\,\underset{\sim}{\beta} \tag{4.6}$$

as in Eq. (3.10). The strain increments are derived as,

$$\{\underset{\sim}{\Delta\varepsilon}\} = \begin{Bmatrix} \Delta\varepsilon_{rr} \\ \Delta\varepsilon_{\theta\theta} \\ \Delta\varepsilon_{r\theta} \end{Bmatrix} = \begin{Bmatrix} \partial\Delta u_r/\partial r \\ \Delta u_r/r + (1/r)\,\partial\Delta u_\theta/\partial\theta \\ (1/r)\,\partial\Delta u_r/\partial\theta + \partial\Delta u_\theta/\partial_r - \Delta u_\theta/r \end{Bmatrix} \tag{4.7}$$

4.1.2 Boundary Displacements for "Singularity" Elements

Along the circumference of each of the present sector shaped singular elements, where 3 nodes are located as in Fig. 1, each of the displacements Δv_r and Δv_θ are assumed in the form:

$$\Delta v_i = a_{1i} + a_{2i}\theta + a_{3i}\theta^2 \quad (i = r,\theta) \tag{4.8}$$

where a_{1i}, a_{2i} and a_{3i} are expressed in terms of the respective displacements at the 3 nodes along the circumference. Since this displacement varies quadratically at the circumference, continuity of displacements at the interface of the present singular elements and the surrounding 'regular' quadratic isoparametric quadrilateral elements is inherently satisfied.

Along each of the two radial boundaries of the singular sector element, on which 4 mode (including the crack-tip as a node) are located, the displacements are assumed as,

$$\Delta v_i = b_{1i} + b_{2i}r + b_{3i}r^2 + b_{4i}r^{1/n+1} \quad (i = r,\theta) \tag{4.9}$$

wherein the coeffecients $b_{1i} \ldots b_{4i}$ are expressed in terms of the respective displacements at the above mentioned 4 nodes. It is seen that the above boundary displacement field along the radial lines is inherently compatible at the interfaces with the adjacent singular elements.

Thus there is interelement displacement compatibility not only amongst the singularity sector elements themselves, but also with the surrounding regular isoparametric elements.

4.1.3 Boundary Tractions for Singularity Element

The boundary tractions T_{Li} for the singular element as defined in Eq. (3.10), which are mathematically the Lagrange Multipliers in the hybrid variational principle as in Eq. (3.4), are assumed as:

$$T_{Li} = \nu_i \, \sigma_{ij} \tag{4.10}$$

where σ_{ij} are derived from an Airy Stress function, ψ, as:

$$\sigma_{rr} = (1/r)\, \partial\psi/\partial r + (1/r^2)\, \partial^2\psi/\partial\theta^2 \tag{4.11}$$

$$\sigma_{\theta\theta} = \partial^2\psi/\partial r^2 \tag{4.12}$$

$$\sigma_{r\theta} = (1/r^2)\partial\psi/\partial\theta - (1/r)\partial^2\psi/\partial r\partial\theta \tag{4.13}$$

and ν_i in Eq. (4.10) denote the direction cosines of a unit outward normal to the boundary. The Airy Function ψ is chosen such that the stress field contains a $r^{-1/n+1}$ type singularity, as:

$$\begin{aligned}\psi = {} & \alpha_1 r^2 + \alpha_2 r^2\theta + \alpha_3 r^2\theta^2 + \alpha_4 r^2\theta^3 + \alpha_5 r^3 + \alpha_6 r^3\theta \\ & + \alpha_7 r^3\theta^2 + \alpha_8 r^3\theta^3 + \alpha_9 r^4 + \alpha_{10} r^4\theta + \alpha_{11} r^4\theta^2 \\ & + \alpha_{12} r^4\theta^3 + \alpha_{13} r^{(2n+1/n+1)} + \alpha_{14} r^{(2n+1/n+1)}\theta + \alpha_{15} r^{(2n+1/n+1)}\theta^2\end{aligned} \tag{4.14}$$

where α's are undetermined parameters. We note that the element boundary traction field as chosen above is self-equilibrated.

4.2 Displacement Field Assumption for Regular Elements

As noted earlier, the region of the cracked structure outside the above discussed singularity core region is modeled with conventional isoparametric displacement elements. An eight node isoparametric quadrilateral finite element, as shown in Fig. 2, is used for this purpose. The transformation from cartesian coordinates of the element, with general quadratic curves as boundaries, to curvi-linear coordinates ξ and η, as indicated in Fig. 2, is achieved through:

$$X = \sum_{i=1}^{8} N_i(\xi,\eta)X_i; \quad y = \sum_{i=1}^{8} N_i(\xi,\eta)y_i \tag{4.15}$$

where, the functions $N_i(\xi,\eta)$ are defined as:

$$N_i(\xi,\eta) = (1/4)(1 + \xi\xi_i)(1 + \eta\eta_i)(\xi\xi_i - \eta\eta_i - 1) \tag{4.16}$$

for corner nodes i = 1, 3, 5 and 7 as indicated in Fig. 2, and

$$N_i(\xi,\eta) = (1/2)(1 - \xi^2)(1 + \eta\eta_i) \tag{4.17}$$

for nodes with $\xi_i = 0$, and, finally,

$$N_i(\xi,\eta) = (1/2)(1 - \eta^2)(1 + \xi\xi_i) \tag{4.18}$$

for nodes with $\eta_i = 0$. The displacement field for the regular element, as defined in Eq. (3.12), is expressed as:

$$\{\Delta u\} = \begin{Bmatrix} \Delta u_x \\ \Delta u_y \end{Bmatrix} = \underset{\approx}{D}\ \Delta q \tag{4.19}$$

where,

$$\underset{2x16}{[D]} = \begin{bmatrix} N_1; & 0; & N_2; & 0; \ldots N_8; & 0 \\ 0; & N_1; & 0; & N_2 \ \ldots 0; & N_8 \end{bmatrix} \tag{4.20}$$

and $\lfloor \Delta q \rfloor = \lfloor \Delta q_1; \ \Delta q_2 \ \ldots \ \Delta q_{16} \rfloor$. From Eq. (4.19), the element strains are defined as:

$$\{\underset{\sim}{\Delta\epsilon}\} = \begin{Bmatrix} \Delta\epsilon_{xx} \\ \Delta\epsilon_{yy} \\ \Delta\gamma_{xy} \end{Bmatrix} = \underset{\approx}{B} \ \underset{\sim}{\Delta u} = \underset{\approx}{B} \ \underset{\approx}{D} \ \underset{\sim}{\Delta q} \tag{4.21}$$

$$\text{where} \quad [B] = \begin{bmatrix} \partial N_i/\partial X & 0 \\ 0 & \partial N_i/\partial y \\ \partial N_i/\partial X & \partial N_i/\partial y \end{bmatrix} \tag{4.23}$$

Finally, we note

$$\begin{Bmatrix} \partial N_i/\partial x \\ \partial N_i/\partial y \end{Bmatrix} = [J]^{-1} \begin{Bmatrix} \partial N_i/\partial \xi \\ \partial N_i/\partial \eta \end{Bmatrix} \tag{4.24}$$

where [J] is the Jacobian of the transformation used in Eq. (4.15).

5. Elastic-Plastic Constitutive Relations

In the present analysis, based on an incremental theory of plasticity, the piecewise linear relation between the stress and strain rates* is taken as:

$$d\sigma_{ij} = \overset{*t}{E}_{ijk\ell} \ d\epsilon_{k\ell} \tag{5.1}$$

where $\overset{*t}{E}_{ijk\ell}$ is the current tensor of elastic-plastic constitutive law; and the total strain rate is assumed to be a sum of elastic and plastic parts,

*First, we develop the constitutive relation for a small-displacement theory of plasticity, and later generalize it for the case of finite deformations.

as:

$$d\epsilon_{k\ell} = d\epsilon^{e}_{k\ell} + d\epsilon^{p}_{k\ell} \tag{5.2}$$

The elastic strain increments are assumed to be given by the Hookes' law as:

$$d\sigma_{ij} = E_{ijk\ell}\, d\epsilon_{k\ell}^{e} \tag{5.3}$$

where $E_{ijk\ell}$ is current elasticity tensor. In the classical rate theory of plasticity, which is used in the present, the elastic-plastic behaviour of the material is fully described by specifying: an initial yield criterion; a flow rate; and a hardening rule. The elastic-plastic constitutive tensor $E^{t}_{ijk\ell}$ is obtained by specifying each of the above, as in the following.

(i) Initial Yield Criterion

The well known J_2 flow theory of Huber-Mises -Hencky is used in specifying the initial yield criterion, which states:

$$f(J_2) = (\tfrac{3}{2})\, \sigma'_{ij}\, \sigma'_{ij} - \sigma^2_{Ys} = 0 \tag{5.4}$$

where σ_{Ys} is the yield stress of the material and σ'_{ij} is the deviatoric stress as defined by

$$\sigma'_{ij} = \sigma_{ij} - \frac{1}{3}\sigma_{kk}\,\delta_{ij} \tag{5.5}$$

$$\delta_{ij} = \begin{cases} 1 \text{ if } i = j \\ 0 \text{ if } i \neq j \end{cases}$$

For the special case of plane stress conditions. The initial yield surface as described by Eq. (5.4) reduces to

$$f(\sigma_{ij}) = \sigma^2_{xx} + \sigma^2_{yy} + \sigma_{xx}\sigma_{yy} + 3\sigma^2_{xy} - \sigma^2_{ys} = 0 \tag{5.6}$$

and for the case of plane strain conditions,

$$f(\sigma_{ij}) = \sigma_{xx}^2 + \sigma_{yy}^2 + \sigma_{zz}^2 - \sigma_{xx}\sigma_{yy} - \sigma_{xx}\sigma_{zz} - \sigma_{yy}\sigma_{zz} + 3\sigma_{xy}^2 - \sigma_{ys}^2 = 0 \tag{5.7}$$

(ii) Flow Rule

The well known Drucker's normality rule, which states that the plastic strain increment is always orthogonal to the yield surface, or

$$d\epsilon_{ij}^p = d\lambda \frac{\partial f}{\partial \sigma_{ij}} \tag{5.8}$$

where $d\lambda$ is a proportionality, is used. If the plastic strain vector is superimposed on the stress or space (as best depicted in Fig. 3), for small increments of stress and strain the relation between the stress and the strain increments and the yield surface will be

$$(d\sigma_{ij} - c d\epsilon_{ij}^p) \frac{\partial f}{\partial \sigma_{ij}} = 0 \tag{5.9}$$

From Eqs. (5.8) and (5.9) the proportionality constant $d\lambda$ is determined as

$$d\lambda = \frac{1}{c} \frac{\left(\frac{\partial f}{\partial \sigma_{ij}}\right) d\sigma_{ij}}{\left(\frac{\partial f}{\partial \sigma_{k\ell}}\right)\left(\frac{\partial f}{\partial \sigma_{k\ell}}\right)} \tag{5.10}$$

where c is a constant.

Substituting the above relation for $d\lambda$ into the Eq. (5.8), now we get a flow rule,

$$d\epsilon_{ij}^p = \frac{1}{c} \frac{\left(\frac{\partial f}{\partial \sigma_{mn}}\right)\left(\frac{\partial f}{\partial \sigma_{ij}}\right)}{\left(\frac{\partial f}{\partial \sigma_{k\ell}}\right)\left(\frac{\partial f}{\partial \sigma_{k\ell}}\right)} d\sigma_{mn} \tag{5.11}$$

For the simplest case of uniaxial tension or compression Eq. (5.11) reduces to,

$$d\epsilon^p = \frac{1}{c} d\sigma, \qquad \text{or } c = \frac{d\sigma}{d\epsilon^p} \tag{5.12}$$

Therefore in the case of the uniaxial loading the parameter 'c' is the slope of stress-plastic strain curve. Or

$$c = \frac{2}{3} H' = \frac{2}{3} \frac{d\sigma_{eq}}{d\epsilon^{p}_{eq}} \tag{5.13}$$

where H' is the slope of the equivalent stress-equivalent plastic strain curve, and σ_{eq} and $d\epsilon^{p}_{eq}$ are defined, respectively, as

$$\sigma_{eq} = \sqrt{\frac{3}{2} \sigma'_{ij} \sigma'_{ij}} \tag{5.14}$$

$$d\epsilon^{p}_{eq} = \sqrt{\frac{2}{3} d\epsilon^{p}_{ij} d\epsilon^{p}_{ij}} \tag{5.15}$$

(iii) Hardening rule

Prager's [21] kinematic hardening low, as modified by Ziegler [22] which appears to adequately model the Bauschinger effects that are generally observed in most of metals under cyclic loading is chosen. In this case, the subsequent yield surface is represented by,

$$f(\sigma_{ij} - \alpha_{ij}) = 0 \tag{5.16}$$

Ziegler's [22] modified kinematic hardening rule states that the translation of the yield surface, $d\alpha_{ij}$, is always in the direction of the vector $\sigma_{ij} - \alpha_{ij}$, ie.,

$$d\alpha_{ij} = d\mu \, (\sigma_{ij} - \alpha_{ij}) \tag{5.17}$$

as shown in Fig. 3. For an infinitesimal increment of loading the vector $d\sigma_{ij} - d\alpha_{ij}$ must be orthogonal to the outer normal to the surface; thus

$$(d\sigma_{ij} - d\alpha_{ij}) \frac{\partial f}{\partial \sigma_{ij}} = 0 \tag{5.18}$$

The scalar quantity $d\mu$ is obtained by substituting Eq. (5.17) into (5.18) to get,

$$d\mu = \frac{\frac{\partial f}{\partial \sigma_{ij}} d\sigma_{ij}}{(\sigma_{k\ell}-\alpha_{k\ell}) \frac{\partial f}{\partial \sigma_{k\ell}}} \tag{5.19}$$

Therefore the rate of the yield surface translation is given by

$$d\alpha_{ij} = \frac{(\sigma_{ij}-\alpha_{ij}) \frac{\partial f}{\partial \sigma_{mn}} d\sigma_{mn}}{(\sigma_{k\ell}-\alpha_{k\ell}) \frac{\partial f}{\partial \sigma_{k\ell}}} \tag{5.20}$$

Upon substitution of $d\varepsilon^p_{ij}$ from Eq. (5.11) into Eqs. (5.2 and 5.3), the relation between the stress rate and the total strain rate can be expressed as follows:

a. for plane stress case:

$$\begin{Bmatrix} d\sigma_{xx} \\ d\sigma_{yy} \\ d\sigma_{xy} \end{Bmatrix} = \begin{bmatrix} \frac{E}{1-\nu^2} - \frac{S_1^2}{S}, & \frac{E\nu}{1-\nu^2} - \frac{S_1 S_2}{S}, & -\frac{S_1 S_3}{S} \\ & \frac{E}{1-\nu^2} - \frac{S_2^2}{S}, & -\frac{S_2 S_3}{S} \\ \text{- sym -} & & \frac{E}{2(1+\nu)} - \frac{S_3^2}{S} \end{bmatrix} \begin{Bmatrix} d\varepsilon_{xx} \\ d\varepsilon_{yy} \\ 2d\varepsilon_{xy} \end{Bmatrix} \tag{5.21}$$

where

$$S_1 = \frac{E}{1-\nu^2}\left(\frac{\partial f}{\partial \sigma_{xx}} + \nu \frac{\partial f}{\partial \sigma_{yy}}\right)$$

$$S_2 = \frac{E}{1-\nu^2}\left(\nu \frac{\partial f}{\partial \sigma_{xx}} + \frac{\partial f}{\partial \sigma_{yy}}\right)$$

$$S_3 = \frac{E}{1+\nu} \frac{\partial f}{\partial \sigma_{xy}}$$

$$S = CQ + S_1 \frac{\partial f}{\partial \sigma_{xx}} + S_2 \frac{\partial f}{\partial \sigma_{yy}} + 2S_3 \frac{\partial f}{\partial \sigma_{xy}}$$

$$Q = \left(\frac{\partial f}{\partial \sigma_{xx}}\right)^2 + \left(\frac{\partial f}{\partial \sigma_{yy}}\right)^2 + 2\left(\frac{\partial f}{\partial \sigma_{xy}}\right)^2$$

$$\frac{\partial f}{\partial \sigma_{xx}} = 2(\sigma_{xx} - \alpha_{xx}) - (\sigma_{yy} - \alpha_{yy})$$

$$\frac{\partial f}{\partial \sigma_{yy}} = 2(\sigma_{yy} - \alpha_{yy}) - (\sigma_{xx} - \alpha_{xx})$$

$$\frac{\partial f}{\partial \sigma_{xy}} = 3\ (\sigma_{xy} - \alpha_{xy}) \qquad (5.22)$$

b. for plane strain case:

$$\begin{Bmatrix} d\sigma_{xx} \\ d\sigma_{yy} \\ d\sigma_{xy} \end{Bmatrix} = \begin{bmatrix} \frac{E(1-\nu)}{(1+\nu)(1-2\nu)} - \frac{S_1^2}{S}, & \frac{\nu E}{(1+\nu)(1-2\nu)} - \frac{S_1 S_2}{S}, & -\frac{S_1 S_3}{S} \\ & \frac{(1-\nu)E}{(1+\nu)(1-2\nu)} - \frac{S_2^2}{S}, & -\frac{S_2 S_3}{S} \\ \text{- sym -} & & \frac{E}{2(1+\nu)} - \frac{S_3^2}{S} \end{bmatrix} \begin{Bmatrix} d\epsilon_{xx} \\ d\epsilon_{yy} \\ 2d\epsilon_{xy} \end{Bmatrix} \qquad (5.23)$$

where

$$s_1 = \frac{E}{(1+\nu)(1-2\nu)} \left\{(1-\nu)\frac{\partial f}{\partial \sigma_{xx}} + \nu \frac{\partial f}{\partial \sigma_{yy}}\right\}$$

$$s_2 = \frac{E}{(1+\nu)(1-2\nu)} \left\{\nu \frac{\partial f}{\partial \sigma_{xx}} + (1-\nu)\frac{\partial f}{\partial \sigma_{yy}}\right\}$$

$$s_3 = \frac{E}{1+\nu} \frac{\partial f}{\partial \sigma_{xy}}$$

$S =$
$Q =$ } are defined to be same as in the plane stress case.

$$\frac{\partial f}{\partial \sigma_{xx}} = \frac{3}{2}\left[(\sigma_{xx} - \alpha_{xx}) - (\sigma_{yy} - \alpha_{yy})\right]$$

$$\frac{\partial f}{\partial \sigma_{yy}} = \frac{3}{2}\left[(\sigma_{yy} - \alpha_{yy}) - (\sigma_{xx} - \alpha_{xx})\right]$$

$$\frac{\partial f}{\partial \sigma_{xy}} = 3(\sigma_{xy} - \alpha_{xy}) \tag{5.24}$$

As noted earlier, the above relation, $d\sigma_{ij} = \overset{*t}{E}_{ijk\ell}\, d\epsilon_{k\ell}$ was derived for a small displacement theory of plasticity.

In generalizing the above relation to finite deformations, one needs to make a choice for an objective stress rate and an appropriate strain rate; and $E^{t}_{ijk\ell}$ can be used as constitutive-relation tensor relating the chosen objective stress-rate and its conjugate strain rate. In [15,16], and elsewhere, the advantages of using the corotational rate of Kirchhoff stress [which is J times the true stress τ_{ij}], (which stress rate is physically the stress increment measured in a coordinate system that is instantansously coincident with the current carstesian system in the updated configuration C_N, but is rotating with respect it at the same rate as the spin suffered by the material fibers in going from $C_N \rightarrow C_{N+1}$), in the elastic-plastic constitutive law for finite deformations have been discussed. If ΔK^{J}_{ij} is the corotational rate of Kirchhoff stress, it is shown in [15,16], that it is related to the Truesdell stress-increment $\Delta^{*}S_{ij}$ of Eq. (3.2), through:

$$\Delta^{*}S_{ij} = \Delta K^{J}_{ij} - \Delta^{*}g_{ik}\tau^{N}_{kj} - \tau^{N}_{ik}\,\Delta^{*}g_{kj} \tag{5.25}$$

where τ^{N}_{kj} and $\Delta^{*}g_{kj}$ are as defined earlier. Now, as discussed above and as elaborated in [15,16], a generalization of the elastic-plastic law can be written as:

$$\Delta K^{J}_{ij} = \overset{*t}{E}_{ijk\ell}\ \Delta^{*} g_{k\ell} \tag{5.26}$$

By substituting Eq. (5.26) in (5.25), the tensor $E^{t}_{ijk\ell}$ in the relation

$$\Delta^{*} S_{ij} = E^{t}_{ijk\ell}\ \Delta^{*} g_{k\ell} \tag{5.27}$$

is found, and is used in the developments discussed earlier, ie., Eq. (3) on words. Finally, we note that in the above generalization for finite deformations, the initial as well as subsequent yield functions are expressed in terms of the true stress, τ_{ij}.

5.1 Knee Correction

Once a point has yielded, the state of stress represented by its location in the stress space stays on the yield surface until unloaded. The subsequent loading condition of the point is determined, by checking $\frac{\partial f}{\partial \tau_{ij}}\, d\tau_{ij}$, as loading, neutral loading, and unloading depending on whether $\frac{\partial f}{\partial \tau_{ij}}\, d\tau_{ij}$ is positive, zero, or negative respectively. However, some complications arise when an elastic or unloaded part of the structure near yield becomes plastic with the next increment of load. A technique, herein called "knee correction", is used for dealing with each integration point in this transition region, of elastic and plastic behavior, and is briefly described in the following.

First an estimate of strain and stress increments which made the point yield is made by assuming,

$$f(\tau_{ij} + \gamma \Delta\tau_{ij} - \alpha_{ij}) = 0 \tag{5.28}$$

where $\Delta\tau_{ij}$ is the total increment of stress obtained for at the present increment of loading, and γ is the proportionality constant so that the increment $\gamma\Delta\tau_{ij}$ causes yield at the point. Solving Eq. (5.28) for γ, $\gamma\Delta\tau_{ij}$ is treated

as if it acts elastically, then subsequently the behavior is assumed to be elastic-plastic, with the remaining strain increment, $(1-\gamma)\Delta^{*}g_{ij}$.

6. Finite Element Modelling of Crack Growth

The steps in the finite element simulation of crack growth in the present procedure may be described as: (i) geometrical change in the crack surface boundary; (ii) translation of the crack-tip singularities to the advanced crack-tip; and (iii) release of surface tractions on the newly created crack surface.

The change in the crack surface boundary is made by translating the whole set of crack-tip core elements, as shown in Fig. 4, by arbitrary distance Δa in the direction of intended crack extension; thus the new crack-tip node which is designated by the center of the sector-shaped core elements need not be coincident with any previously existing finite element node before extension. Thus even though the fixed boundary in the uncracked ligament of the structure is changed, the constraining condition of the nodes need not be altered. Elements immediately adjacent to the core must be re-adjusted to fit to the translated core. This process of translating the core mesh also moves the embedded singularity in the elements to the new crack tip area, leaving no singularities but large deformations and strains in the wake of advanced crack-tip. All the 5x5 Gaussian data points in each of the translated core element (and also the 5x5 points for the conventional elements) may generally not coincide with those before translation, at which plastic history data such as current stresses, plastic strains, plastically dissipated work, yield surface translation, etc., are available. Therefore the data at points in the new mesh are estimated by linearly interpolating data on four Gaussian points in the old mesh that are nearest to the point

under question in the new mesh. The simple but cumbersome mathematical details of this interpolation and smoothing process are omitted here for the sake of brevity. With the fitted plastic data and the new element geometry, element stiffness matrices are recalculated for the core elements as well as for the surrounding rearranged elements and the global stiffness is appropriately modified. Subsequent equilibrium check iterations using the new stiffness of the structure correct fitting errors, if any, in the plasticity data in the new mesh. At the same time, the tractions over the distance AB (Δa as shown in Fig. 4) are incrementally removed, with equilibrium check iterations being used at each step, to create a new traction-free crack surface of length Δa. The finite element simulation of crack extension by the desired amount, Δa, is now completed.

7. Analysis of Fatigue Crack Growth Under Mode I Cyclic Loading

7.1 Description of the Problem

Through out the series of the present elastic-plastic finite element analyses of fatigue crack growth under Mode I type cyclic loading, a thin rectangular plate with a central crack and under uniform tensile stresses, in a direction normal to the crack-axis, at the edges of the plate, is considered (See Fig. 5). The dimensions of the plate are: half width w = 230mm; and half-crack length a_o = 27.3mm, respectively. The material is considered to be a 2024-T3 Aluminum alloy, whose mechanical properties are characterized by: yield stress, σ_{ys} = 350 MN/m^2; and Young's modulus, E = 70,000 MN/m^2. The material is assumed to be elastic-perfectly-plastic. It is noted that the above problem definition is identical to that used by Newman [8]. The plate is assumed to be in a state of plane stress.

Because of the symmetries of geometry, applied loading, and material homogeneity, only a quarter of the cracked plate is analysed. Fig. 5 shows the finite element breakdown that is used. A total of 6 sector-shaped singularity elements near the crack-tip, and 43 conventional quadratic isoparametric elements are employed. Some of these isoparametric elements are 6 noded triangles, while the majority are 8 noded quadrilaterals (See Fig. 5). It is seen that the total number of nodes in the finite element mesh for the quarter-plate is 171, with a total number of degrees of freedom of 311.

The radius of the sector-shaped singularity elements is chosen as ρ = 2.8mm; ie., ρ/a_o = .103. While the crack-extension per cycle of loading, Δa, can be arbitrary (ie., not related to the finite element mesh size) in the present analysis procedure, it is chosen to be Δa = 0.14mm in the present series of computations.

7.2 Techniques to Minimize Computational (CPU) Time

Firstly, we note that the near-tip elements used presently are of the order 10^{-1} times the semi-crack length; and the total number of algebraic equations for the above problem are only 311.

In the present procedure, a tangent modulus (stiffness) approach is used in each increment and in each iteration in the respective increment. Thus a faster convergence is obtained in the process of iterations of equilibrium correction, etc. However, it is noted that only the stiffness matrices of the plastic portion of the structure need to be changed in the present tangent modulus approach, whereas, those of the elastic portion remain fixed.

For the presently considered levels of applied far-field tension on the specimen, only "small-scale" yielding conditions prevail near the crack-tip.

A typical plastic-zone size near the crack-tip for the presently considered class of Mode I problems is shown in Fig. 6a, being superimposed on the finite element mesh. It is seen that the plastic portion of the structure (designated "Region P") is considerably smaller than the elastic portion (designated "Region E"). Thus only the stiffness matrix of region P need to be changed in each load-step and each iteration in the present procedure.

However, the total number of times, say N, that the combined stiffness matrix (for Regions P + E) must be inverted in the course of analyzing a typical problem, say the case a growing crack under constant amplitude cyclic loading, is N = [(no. of iterations/cycle) X (number of load increments per cycle) X no. of load cycles]. For a typical problem, say 8 cycles of constant amplitude loading, a typical value for N can be N = 4 x 28 x 8 = 896, (ie., 4 iterations per cycle, with 28 load increments/cycle, etc.). This is a rather enormous amount of computing; and hence a more economical way of solving the stiffness equations is mandatory.

Since the plastic-zone is a small-size, by an appropriate node numbering scheme, the stiffness matrix of the plastic zone can be arranged, as in Fig. 6.b, so that it is a small sub-set of the global stiffness matrix of the structure (eventhough the plastic zone size keeps changing with load, an approximate preliminary analysis can be made to determine its size at maximum load). Then we use a static condensation procedure to first eliminate the equations corresponding to the nodes in the elastic portion, in the very first load-increment. Thereafter only the equations for the nodes in Region P need to be operated upon, in all subsequent load steps and iterations. Thus, in the example cited above, (N = 896), in all but one of the 896 solutions, the number of equations being solved is rather very small, and correspond to the total number of unconstrained nodal

displacements in Region P. This enables the present computations to be economically feasible.

Also, the computer program is so arranged that the data obtained from computation upto the end of a given spectrum of loading can be used as input data at the beginning of a different spectrum of loading. For instance, at the end of a constant Hi-amplitude cyclic loading, the data is stored on a direct access permanent disc file and used as initial conditions for a low amplitude cyclic load specturm; in this process not only the case of Hi-amplitude loading but also the case of Hi-to-Lo block loading is solved.

7.3 Monitoring of Crack-Closure and -Opening in the Finite Element Model

Let us assume, that at a given instant of time (at a given point in the loading history), the location of the crack-tip, the location of the 4 nodes on the radial line (which coincides with the crack surface) of the singular sector element, the locations of all other nodes on the crack axis, as well the current (deformed) profile of the crack surface, are all known.

We denote the current nodes on the crack surface as "Updated Lagrangean Nodes". Let us now assume that the crack-tip is now further extended by an arbitrary amount (Δa) and the structure is then subjected to further loading. We first note that, in the present development, the boundary displacement (in the direction of the applied normal stress) along a radial line of a "singular" sector element is of the form,

$$\Delta v_y = a\, r^{1/n+1} + br^2 + cr + d \qquad (7.1)$$

where a, b, c, and d are expressed in terms of the normal displacement, Δv_y, of each of the 4 nodes on the radial line of the sector element in its current location. Using the above equation, and knowing, a priori, the

radial coordinates, (ie., r, as measured from the current crack-tip), of the respective nodes on the radial line of the sector element in its immediately previous location, one can compute the values of Δv_y at the above mentioned "Updated Lagrangean Nodes". By adding (or substracting, as the case may be,) these incremental displacements to the previously known values, an accurate prediction of the current crack surface deformation profile is made.

During the unloading part of any cycle, of the present cyclic loading case, at the instant the displacement (in the direction of applied tension) at one or more nodes on the crack surface becomes negative, further unloading stopped. The computational procedure is then switched to a displacement control type, and the above negative displacements are precisely enforced to be zero; thus finding the precise stress level at which the closure constraint on the respective node must be enforced.

After the crack-closure is detected, the respective node(s) are constrained thereafter, until the restraining force(s) at the node(s) just becomes zero and begins to be tensile in nature. The corresponding applied stress level defines the crack-opening stress.

The above processes are illustrated for the case of constant amplitude cyclic loading in Fig. 7; in which, the vertical displacement (when the crack is open) and the restraining force (when the crack closes) at a node, at which the crack closes and opens, are plotted against the applied stress level. It can be seen from Fig. 7 that the crack-opening stress σ_{op} (or the closure stress $\sigma_{c\ell}$) can be most accurately determined by extrapolating to zero the respective nodal displacement after opening (or just before closure, to find $\sigma_{c\ell}$), as well as by extrapolating to zero the restraining force at the respective node just before opening (or just after closure to

find $\sigma_{c\ell}$). It can be seen that the values σ_{op} and $\sigma_{c\ell}$ obtained by the above two sets of extrapolation procedures agree excellently. This indicates that the present numerical procedure of determining σ_{op} and $\sigma_{c\ell}$, by monitoring crack-surface displacements and the nodal restraining forces, is very accurate.

Finally, some comments on the presently observed patterns of crack-closure are given, before proceeding to a discussion of specific cases. In general, closure was noticed to occur at the node closest to the current crack-tip, as indicated in the sequence of unloading steps in Figs. 8a-c. However, if the current crack-sruface profile is irregular, as in the case of Hi-to-Lo block loading to be discussed later, crack-closure may first occur at the node closest to the crack-tip; however, in the subsequent unloading step, closure may occur at a node far-removed from the crack-tip, as indicated in Fig. 8d. From the results to be discussed later, this pattern of crack-closure appears to contribute significantly to growth retardation and delay effects.

7.4 Criterion For Crack-Extension Stress Level

In the present work, a study is made to arrive at a criterion for the stress level, σ_{ex}, at which fatigue crack growth occurs. In prior literature, this crack-extension stress level was chosen arbitrarily. For instance, in [8] the crack is extended at the maximum applied stress in each cycle even in a general spectrum (for instance, high-to-low, low-to-high, etc.,) loading, where as in [10] the crack was extended at the applied stress level at which the restraining nodal force at the new crack-tip becomes zero. In the present study, for instance in a constant-amplitude (zero-to-tension) cyclic loading, it was found that the crack opening and closure stresses,

σ_{op} and σ_{cl} respectively, were sensitive to the chosen σ_{ex}.

In the present work, a criterion, $\sigma_{ex} = \sigma_{op} + p(\sigma_{max} - \sigma_{op})$, where p is a constant of proportionality, is postulated; and p is obtained by calibration such that the calculated σ_{op} correlated with that observed in experimental studies such as in [1,2,3]. However, it is noted that this constant of proportionality p may, to some extent, be dependent on the numerical methodology employed in fatigue crack modeling itself. Thus the above described calibration may be considered as valid only in the context of the particualr methodology employed in the present work.

Three different test cases, each with a different magnitude of constant amplitude (zero to tension) cyclic loading, were studied with different values being chosen in each case for the above mentioned constant of proportionality, p. The idea was to select a 'p' that yields results, in each case, for $(\sigma_{op}/\sigma_{max})$ that are in best agreement with the experimental results [1,2,3] for 2024-T3 Aluminum alloy, which is the material simulated in analysis.

The results, for instance, for the case $(\sigma_{max}/\sigma_{ys} = .40)$ and $(R = \sigma_{min}/\sigma_{max} = 0)$ are summarized as follows:

p	Levelled-off σ_{op}	$[\sigma_{op}/\sigma_{max}]$ at steady state
1.0	115 MP_a	.82
.85	94 "	.67
.62	79 "	.56
.40	58 "	.41

Similar results were obtained for the cases, $(\sigma_{max}/\sigma_{ys}) = .229$ and $(\sigma_{max}/\sigma_{ys}) = .314$. From these three sets of results, it was observed that $p \sim 0.62$ yields results for $(\sigma_{op}/\sigma_{max})$ that are in best agreement with experimental observations, which indicate that $[\sigma_{op}/\sigma_{max}]$ at steady state is about 0.56.

Thus when p is chosen to be 0.62, the results obtained for the steady state vaule of $(\sigma_{op}/\sigma_{max})$ for three-different cases of $(\sigma_{max}/\sigma_{ys})$ are summarized as follows:

Case No.	σ_{max}/σ_{ys}	Levelled off σ_{op}	$(\sigma_{op}/\sigma_{max})$, steady state
1	0.229	44 MP_a	0.55
2	0.314	57.5 MP_a	0.52
3	0.40	78.5 MP_a	0.56

It is hypothesized that the above constant p = 0.62 may be used throughout the rest of the analysis, ie., for cases of general spectrum loading. We also note that when the load level σ_{op} during any cycle is first determined, the number (and size) of load steps between this σ_{op} and σ_{max}, in the respective cycle, is so adjusted that the pre-chosen level of $\sigma_{ex}[= \sigma_{op} + p(\sigma_{max} - \sigma_{op})]$ coincides with one of the load-increments in the cycle.

We now discuss the results of analysis of each of the loading cases.

7.5 Constant Amplitude Zero-to-Tension Cyclic Loading

(i) The results for σ_{op}, for the case of $(\sigma_{max}/\sigma_{ys}) = 0.4$ and $R = (\sigma_{min}/\sigma_{max}) = 0$, are shown in Fig. 9, for 8cycles of loading. It is observed that σ_{op} reaches a "steady-state" value of 0.56 σ_{max} after the 4^{th}

or 5^{th} cycle. It is also noted that this value for σ_{op}/σ_{max} (= 0.56) is in reasonable accord with experimental results [1,2,3] for the same material, a 2024-T3 Aluminum alloy.

(ii) From Fig. 7, wherein the opening displacement and restraining force at a node, at which crack-closure occurs, are plotted against the applied stress, a nonlinearity in the variation of the opening displacment, as the load approaches σ_{max} (for instance, between points D-E in Fig. 7) is observed; this can be seen to be due to plastic deformation. In the subsequent unloading (from point E in Fig. 7) the opening displacement decreases linearly, thus showing the effects of elastic unloading. When crack closure occurs (point F in Fig. 7), a nonlinearity in the variation of the nodal-restraining force (between F-G) can be noticed until the applied stress in the cycle becomes zero; this reflects plastic compression.

(iii) Knowing σ_{op} in each cycle, we define the effective stress-intensity factor as:

$$\Delta K_{eff} = C_1 \sqrt{\pi(a_o + N\Delta a)}\ (\sigma_{max} - \sigma_{op}) \qquad (7.2)$$

where C, is the finite-size correction factor for the present crack geometry (which was found to be $C_1 = 1.017$ from a finite element linear analysis of the crack with $a = a_o$; and thereafter assumed to be constant); N is the number of cycles and Δa is the crack growth per cycle. For convenience, the variation of ΔK_{eff} is plotted against a, the current crack length, in Fig. 10. It is seen that ΔK_{eff} levels-off after a few cycles to a steady state value.

(iv) Fig. 11 shows the crack surface deformation profiles, for instance, at various stages of unloading during the 8^{th} cycle of the present constant-amplitude (R = o) cyclic loading. The large blunting at the initial

crack-tip location ($a = a_o$) is observed to remain permanently. The surface of the extended crack is observed to be fairly smooth. During the 8^{th} cycle, it is observed that precise crack-closure occurs only over the area Δa (ie., only at the previous location of the crack-tip node) even upon full unloading; however, it is also noted that at this stage, the opening of the crack faces between the points a_o and the precisely closed node is very small (See Fig. 11).

Lo-To-High Block Loading

A two level block loading, from low to high, with σ_{max} in the higher level being 1.273 times the σ_{max} in the lower level, is considered. The maximum stress in the lower level is taken such that $(\sigma_{max})_{Low} \div (\sigma_{ys}) = .314$. As mentioned earlier, the data at the end of 4 cycles of low level block loading (See Fig. 12) is recovered from a constant-amplitude test case, with the corresponding stress level. The following results were obtained:

(i) The variation of crack-opening stress, σ_{op}, as the cyclic loading progresses, is shown in Fig. (12). It can be seen that immediately after the step up in the level of applied stress, σ_{op} decreases by about 33% of its steady state value corresponding to the lower level of block loading. Subsequent to this, σ_{op} increases monotonically to a steady state value corresponding to the higher level of block loading, within about 5 cycles. Prior to this stabilization, ΔK_{eff} in the higher level of block loading remains considerably higher than the steady state value corresponding to this stress level; thus indicating growth acceleration following the load step-up.

(ii) The variation of ΔK_{eff} with N, with ΔK_{eff} being defined as earlier, is shown in Fig. (13). It is seen that there is a jump in ΔK_{eff} immediately following the step-up in the level of applied loading; thereafter ΔK_{eff}

decreases monotonically down to its base line value corresponding to the higher level block loading, but doesn't go below this base line value. This appears to indicate that the growth rate of the crack, initially growing at a steady rate corresponding to the lower level blocking loading, suddenly accelerates and then smoothly shifts down to a steady state rate corresponding to the higher level block loading.

(iii) The representative crack surface profiles for instance, at various stages of unloading at the end of the 8^{th} cycle (high stress) of the current low-to-high level block loading, are shown in Fig. (14). From this Figure, it can be seen that the step-up in the level of loading causes a blunting of the crack-tip (ie., at the location $x/a_o = 1.02$ in Fig. (14), when the step-up in loading occurs in the present finite element simulation). Even during the unloading at the end of the present two level block loading, as seen from Fig. (14), the crack-closure occurs only over the area Δa (ie., only at the previous location of the crack-tip node).

High-To-Low Block Loading

After 8 consequitive cycles of a high level block loading (the data at which point is recovered from the corresponding constant amplitude test case), the σ_{max} is reduced by 21.4% and 8 more cycles of this reduced level block loading were considered. The magnitude of the applied stress in the high-level block was such that $(\sigma_{max})_{high} \div \sigma_{ys} = 0.40$. The following results were obtained.

(i) The variation of the crack-opening stress σ_{op}, as the loading progresses, is shown in Fig. (15). It is seen that immediately after the step-down in the load level, no abrupt decrease in σ_{op}, as was the case in Low-to-High loading, occurs in the present High-to-Low block loading case.

After the load-level step down, σ_{op} stayed at about 0.70 $(\sigma_{max})_{low}$ within the number of cycles of low-level load considered presently. It may be possible that, as further number of low-level load cycles are considered and the crack-tip grows further and eventually surpasses the plastic zone created during the high level block loading, the σ_{op} decreases to a base line value corresponding to the lower level block loading. However, limitations of computer funds precluded the possibility of considering a larger number of load cycles at the low level.

(ii) The ΔK_{eff} versus N curve (plotted for convenience as ΔK_{eff} vs a/a_o for the present case is shown in Fig. (16). It is seen that after the load-level step down, ΔK_{eff} remains remarkably lower than its base line value corresponding to the low-level block loading; thus indicating the presence of a considerable retardation of growth, but no delay.

(iii) Fig. (17) shows the crack surface profiles during various stages of unloading in one of the low-level cycles of the present Hi-to-Lo block loading. It is seen that at the stage of unloading indicated by point 'B' in Fig. (17), the crack closes only at the previous crack-tip (closure area = Δa). Further unloading, represented by point C, causes another node away from the current crack-tip to close, as seen in Fig. (17). The area of crack-closure thus increases as the unloading progresses.

To understand the effects of the features of crack-closure as in the present case, the problem was reanalysed with the constraint of closure being removed on the node (as discussed above) far away from the crack-tip, but leaving the closure-constraint on the node closest to the crack-tip. The corresponding changes in σ_{op} are indicated by a broken line in Fig. (15); while the change in ΔK_{eff} is also indicated by a broken line in Fig. (16).

These results indicate the influence of properly imposing the closure-constraints on nodes even far away from the crack-tip; when the considered loading, as the present Hi-to-Low case, causes such a type of crack-closure.

Single Over Load

The case of a single overload after 4 cycles of a constant amplitude block loading, followed by further cycles of constant amplitude (equal in magnitude to that before overload) was considered. The following three cases were considered.

Case	Base σ_{max}	σ overload $\div$ $\sigma_{max,\ base.}$	$\frac{\sigma_{op_{max}} - \sigma_{op.base}}{\sigma_{max\ base} - \sigma_{op.base}}$
1	110 MP_a	1.273	0.151
2	110 MP_a	1.455	0.283
3	80 MP_a	2.0	0.681

In the above, $\sigma_{max.base}$ is the maximum applied stress prior to or after overload; $\sigma_{overload}$ is the overload stress; $\sigma_{op.max}$ is the maximum calculated value for crack-opening stress after overload; and $\sigma_{op.base}$ is the base line opening stress for an otherwise constant-amplitude cyclic load at level $\sigma_{max.base}$, and all these stresses are illustrated in Fig. (18a). The obtained restuls are discussed below:

(i) The variations of σ_{op} during the load cycling, for the three different ratios of stress-overload, are indicated in Figs. (18a,b,c) respectively. In all the three overload cases, an abrupt decrease in σ_{op} (which relative

decrease becomes more predominant as the overload stress-ratio increases) is noticed immediately after the single overload application. After this, in all the three cases, σ_{op} increases again to reach a peak value $\sigma_{op.max}$ before levelling off a steady-state value. This relative values of σ_{opmax} increases as the overload stress ratio increases. Also as the overload stress-ratio increases, the later is the occurance of this $\sigma_{op.max}$. For instance, for the overload stress-ratio of 1.273, σ_{opmax} occurs in the 4^{th} cycle after overload (Fig. 18a); for overload ratio of 1.455 this occurs in the 8^{th} cycle after overload (Fig. 18b); while for the case of overload-rato 2.0, σ_{op} is still increasing (Fig. 18c). This implies that the higher the overload ratio is, the more remarkable both the retardation and delay effects are.

(ii) The curve depicting the variation of the ratio $(\sigma_{opmax} - \sigma_{op.base})/(\sigma_{maxbase} - \sigma_{opbase})$ with the overload stress-ratio, which is drawn using the above discussed 3 data points, is shown in Fig. (19). By extrapolation, the threshold value of the overload ratio, at which retardation effects come into play, is seen to be about 1.10. In contrast, Bernard et.al [23] report a threshold overload ratio of $1.3 \sim 1.4$ based on a series of experiments on the material Ducol W30B whose yield strength is 366 MP_a (, comparable to the presently considered $\sigma_{ys} = 350MP_a$). It is noted however, that the present analysis is based on a plane-stress assumption, while Bernard et.al [23] note the dependence of the experimentally determined threshold value on the specimen thickness.

(iii) The variation of ΔK_{eff} with N (or a/a_o) for the single-overload, case, with a ratio of 2, is shown in Fig. (20), with a similar variation being noted for the other two overload cases considered. It is seen that ΔK_{eff} experiences a sudden jump immediately after the overload, and then

decreases below its base line level corresponding to a constant-amplitude cycling at $\sigma_{max,base}$ level; thus indicating the presence of retardation and delay effects (these terms are used here in the same sense as defined by Barnard, et.al [23])in this single overload case. It is also noted that the quantitative effects of retardation and delay depend on the overload ratio.

(iv) The crack-line deformation profiles at various stages of unloading at the end of the considered number of cycles are shown in Fig. (21) for the case of overload ratio of 2, while similar results were noted for the other two overload-ratio cases also. It is seen that the application of the single overload to the specimen (at the instant when $a/a_o = 1.02$ in Fig. 21) causes a large (plastic) blunting which is retained in the crack-surface profile even as the crack advances in further cyclic loading. When the specimen is fully unloaded, at the end of the cycle illustrated in Fig. (21), almost the whole surface area ahead of the previously mentioned location of blunting is noticed to close, while the crack surface area behind this blunting location is seen never to close.

8. Analysis of a Center-Cracked Specimen under Pure Mode II Cyclic Loading

A center cracked square plate under a constant amplitude cyclic loading of pure shear, which is uniformly distributed at the edges of the plate, is analysed. Plane stress conditions are assumed. The material is considered to be 2024-T3 Aluminum alloy, (same as in the Pure Mode I case discussed earlier). The dimensions of the plate are: $L = W = 140mm$; $a_o = 40mm$. The maximum amplitude of the uniformly distributed shear is taken to be $\tau_{max} = 80\ MP_a$ ($\tau_{max}/\sigma_{ys} = .23$).

In the present problem, the geometry of the plate with the crack is symmetrical about both the x and y axis (See Fig. 22), and the external loading in anti-symmetric with respect to both x and y axis.

As earlier, the present material is modeled as an elastic-perfect-plastic material. We note also that the presently considered material has the same properties in tension as in compression.

Thus, the displacement field has the following antisymmetric properties:

$$u_x(x,y) = -u_x(x,-y) = u_x(-x,y) = -u_x(-x,-y) \tag{8.1}$$

$$u_y(x,y) = -u_u(-x,y) = u_y(x,-y) = -u_y(-x,-y) \tag{8.2}$$

where u_x is the displacement in x direction, etc. Further, it is noted that these displacements may be discontinuous at the crack surface, $-a_o < x < a_o$. Thus, in the finite element modeling, only a quarter of the plate is modeled (as shown in Fig. 22) with the displacement boundary conditions: $U_x = 0$ along $y = 0$, in the uncracked ligament only; and $u_y = 0$ at nodes along $x = 0$.

The linear elastic results, based on the first load increment, from the present finite element analysis indicate:

$$K_I = 0.075; \qquad K_{II} = 3.777 \tag{8.3}$$

which compare favorably with the following results (obtained by using the finite-size correction factors of) Bowie and Neal [24] for an identical problem:

$$K_I = 0.0 \qquad K_{II} = 3.899 \tag{8.4}$$

The fact that $K_{II} \neq 0$ in the present finite element analysis is the result of inherent numerical errors, such as round-off and truncation, in the finite element analysis.

Also, to check the numerical accuracy of the present finite element modeling, a second run was made wherein a half of the plate was modeled,

as shown in Fig. (23), instead of only a quarter of the plate. In this model, u_y was set to zero at nodes along $x = 0$, along with constraints to suppress the other two rigid body motions of the plate as a whole. Both the sets of results (ie., those when a quarter and a half of the plate, respectively, are modeled) correslated excellently.

In Fig. (24a) the results for the displacements u_y at the upper and lower crack surfaces, u_y^u and u_y^ℓ respectively, are plotted for the linear elastic case. These numerical results for u_y^u and u_y^ℓ are identical in the linear elastic case. This equality of u_y^u and u_y^ℓ is noticed as the loading continues in the first cycle (crack being stationary) and when the plastic zone size is significant at $\tau = 70$ MPa (see Fig. (25) for the shape of the plasticity zone at $\tau = 70$ MPa).

For lack of any other criteria, the crack was extended, in the present procedure, at 70 MPa (the maximum applied stress being 80 MPa), in the direction of the initial crack ie., in the x-direction. It is seen from Fig. (24a) that significant increase in u_y is brought about by the process of crack extension and hence the attendant plastic unloading; however, again, u_y^u and u_y^ℓ are almost identical (to the 4^{th} significant digit). Thus it is seen that through the all stages of loading, crack extension and plastic-unloading, and further loading (to 8 MPa in this case) after crack extension the upper and lower crack faces experience identical displacements in the y direction, ie., perpendicular to the initial crack axis.

On the other hand, the displacements u_x at the upper and lower surfaces of the crack, u_x^u and u_x^ℓ are plotted in Fig. (24b) for the cases of loading when linear-elastic conditions prevail ($\tau = 31.1$ MPa); when appreciable plasticity develops at the crack-tip ($\tau = 70$ MPa), when the crack is extended (and hence there is plastic loading) at $\tau = 70$ MPa, and when the load

is further increased to 80 MPa after crack extension. It is seen that the magnitudes of u_x^u and u_x^ℓ are nearly identical (to the 4^{th} significant digit), but with opposite sign, in all the above cases. However it is interesting to observe that the change (as a ratio of the respective value prior to crack extension, at the same load) brought about by the process of crack extension (and hence plastic unloading) in u_y is much more pronounced than in u_x.

It is interesting to note that in the linear elastic case the crack-surface displacements u_y^u and u_y^ℓ (see Fig 24a) exhibit almost a linear variation from the crack-tip; thus indicating a lack of any r^α (in particular, $\sqrt{r}$ type for linear elasticity) component in u_y for the linear elastic case. On the other hand, for the linear elastic case, the tangential displacements u_x^u and u_x^ℓ (See Fig. 24b) do exhibit a $\sqrt{r}$ behavior near the crack-tip, for the present Mode II problem. Also, it is seen from Fig. (24b) that, as plasticity develops, the tangential displacements u_x^u and u_y^ℓ exhibit a r^α ($\alpha < 1/2$; and specifically $\alpha = 1/n+1$ as corresponding to Eq. (4.3)) variation near the crack-tip. However, for the pure Mode II case, even in the presence of plasticity, the analyses of Hutchinson [11] and Rice and Rosengren [12], indicate that there may not be a r^α ($\alpha < 1/2$) type variation in u_y near the crack-tip. But the present results for u_y in the presence of plasticity, Fig. 24a, are seen to contain such an $r^\alpha(\alpha < 1/2)$ type variation near the crack-tip. However, it should be noted that the angular variation of the singularity functions, $\bar{u}_i(\phi)$, as embedded in the present sector elements (See Eq. (4.3)) are being approximated as quadratic polynomials in each sector element (See Eqs. 4.4 and 4.5). The fact that $r^\alpha(\alpha < 1/2)$ type variations in u_y are numerically obtained along the radial line of the sector element lying on the crack sruface, as in Fig. 24a,

suggests that the above angular variations are not being solved highly accurately in the present numerical method. However, it appears that these numerical errors are identical at $\phi = +\pi$ as well as at $\phi = -\pi$, so that $u_y^u = u_y^\ell$ as in Fig. (24a).

Finally the crack surface displacements (u_y^u, u_y^ℓ) and (u_x^u and u_x^ℓ) at the end of the first cycle of loading (ie., when the applied stress is brought back to zero) are also indicated in Figs. (24a) and (24b) respectively. Once again it is seen that even after complete unloading, u_y^u and u_y^ℓ are identical in magnitude and direction, where as u_x^u and u_x^ℓ are identical in magnitude but opposite in direction.

Thus for the present material, with identical properties in tension as in compression, it is seen that in all cases of pure-shear type external loading, the upper and lower surfaces of the crack move together in the direction perpendicular to the initial crack-axis, whereas they slide past one another in the direction of the crack-axis. Thus, it appears for these types of materials the phenomenon of crack-closure, as observed experimentaly and as analysed presently in Mode I type loading conditions, does not occur in pure Mode II type cyclic loading.

However the present experience indicates that crack-closure may occur even in pure Mode II cyclic loading if the material has different properties in uniaxial tension and compression. Consideration of such materials is not pursued in the present work.

Finally, the computed shapes and sizes of the plastic zone near the crack-tip at various stages of pure shear loading are indicated in Fig. (25).

9. SUMMARY AND CONCLUSIONS

Based on the results discussed so far, the following observations and conclusions appear to be possible:

(i) If one assumes that the crack-growth-rate, da/dN, in fatigue-loading of Mode I type, is related to the effective stress-intensity factor in the form:

$$\frac{da}{dN} = c(\Delta K_{eff})^n \tag{9.1}$$

where $\Delta K_{eff} = c_1 \sqrt{\pi a}\ (\sigma_{max} - \sigma_{op})$ and n is an exponent, the present results for 4 illustrative types of block loading indicate that: (a) growth retardation occurs in Hi-to-Low and single overload cases, and acceleration in Lo-to-Hi block loading, (b) significant delay effects prior to retardation are observed in the case a single-overload in an other wise constant amplitude cyclic loading.

(ii) The crack-surface deformation profiels, in the different Mode I loading cases, viz., constant amplitude, Lo-to-Hi, Hi-to-Lo, and single overload, have distinctly different characterstic shapes as sketched below:

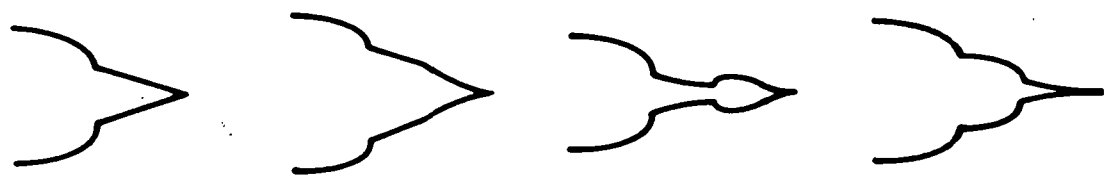

Schematic Representation of Typical Crack-Surface Profiles in Different Cases of Applied Cyclic Loading.

Each of the above crack surface deformation profiles leads to a different pattern of crack-closure when the specimen is unloaded. In the cases of Lo-to-Hi loading and single overload, a considerable amount of crack-surface blunting occurs at the instant when the applied load is stepped up. This blunting precludes the possibility of crack-closure behind the location of this blunting in the subsequent load cycling (in the cases of Lo-to-Hi and single overload). Thus in these two cases of loading, immediately after the step-up in load level takes place, crack closure occurs only in the small area adjacent to the current crack-tip. Consequently, the total compressive force acting on the closed surfaces in these two cases, is also small immediately after the load step-up as shown in Figs. (26) and (27) respectively. In Fig. (26), the maximum opening displacement, in each cycle (ie., at maximum applied load indicated, for instance, by point A in Fig. 26) at the node closest to the current crack-tip, as well as the total compressive force over the closed area of the crack upon total unloading in each cycle (such as at point B in Fig. 26) are shown for the case of Lo-to-High loading; while similar results are shown in Fig. (27) for the case of single-overload. In both the cases, it is seen that the total compressive force over the closed crack-surface becomes a minimum right after the step up in the applied load; thus resulting in a lower value of σ_{op} at which the crack-opens in the tensile portion of the subsequent loading cycle. These phenomona, brought about essentially by a smaller area of crack-closure (due to crack-blunting that occurs at the instant of load step-up), may be responsible for the 'delay' effects - such as, the delayed retardation in the single overload case, and the delayed transition of opening stress levels from the base-line value for lower amplitude block loading to the higher base-line value for the higher

amplitude block loading (see Fig. 13) in Lo-to-High loading case.

(iii) As mentioned, growth retardation occurs in the cases of single overload and Hi-to-Low block loading. Observing the crack-surface profiles for the forementioned two cases, at the instant of complete unloading in a cycle, several cycles after the initial overload, as shown in Figs. (21) and (17), respectively, it is seen that the area of crack closure for both the cases is much larger in comparison with the other two cases (see Fig. 11 and 14). Consequently, the total compressive force in the closed crack-surface is relatively larger in the single-overload and Hi-to-Lo cases than in the other two cases. Thus, in the single overload and Hi-to-Lo cases, after the change in applied level, the crack-opening stresses level off at a much higher value than the baseline value corresponding to the level of applied loading after the formentioned change in loading level.

From these observations, it appears that the pattern of crack-closure has a significant effect on growth retardation in general spectrum loading.

(iv) The crack surface profiles for the Hi-to-Lo loading case, several cycles after the load-step down as shown in Fig. (17), possess certain novel features. Crack closure is seen to be possible not only at the node closest to the crack-tip, but also nodes for removed from it, with no closure being observed at nodes in between. In this case also, growth retardation was found to be possible.

(v) Thus, a correlation between the process of a significant crack-blunting at the instant of transition in the amplitude of applied load-transition, and the possibility of growth retardation is found to exist, as summarized below.

Loading Case	Blunting of Crack at Load-Transition	Dip in σ_{op} in the Subsequent Cycle	Delay	Area of Crack Closure	Retardation/ Acceleration
Constant Amplitude	NO	NO	NO	Small	NONE
Lo-to-Hi	YES	YES	YES	Small	Acceleration
Hi-to-Lo	NO	NO	NO	Large	Retardation
Single Overload	YES	YES	YES	Large	Retardation

The phenomenon of crack-closure was not observed in the present numerical modeling of a thin-center-cracked sheet (of an elastic-perfect-plastic material with identical properties in uniaxial tension as in compression) subject to external pure shear (Mode II) cyclic loading of constant amplitude. The implication of this in the more general problem of fatigue crack growth under mixed-mode cyclic loading deserves further study.

REFERENCES

1. Elber, W., "Fatigue Crack Closure Under Cyclic Tension," Engineering Fracture Mechanics, Vol. 2, No. 1, July 1970, pp. 37-45.

2. Elber, W., "The Significance of Fatigue Crack Closure," Damage Tolerance in Aircraft Structures, ASTM STP 486, 1971, pp. 230-242.

3. Rueping, J. E., Hillberry, B. M., Mettler, S. C., and Stevenson, W. H., "Comparative Study of Fatigue Crack Closure," AIAA Journal, Vol. 16, No. 4, Apr. 1978, pp. 413-415.

4. Fatigue Crack Growth Under Spectrum Loads, ASTM STP 595, American Society for Testing and Materials, 1975, pp. 281-302. (All the papers in it).

5. Budiansky, B. and Hutchinson, J. W., "Analysis of Closure in Fatigue Crack Growth". Journal of Applied Mechanics Vol. 45. No. 2, June 1978, pp. 267-276.

6. Newman, J. C., Jr. "Finite-Element Analysis of Fatigue Crack Propagation-Including the Effects of Crack Closure." Ph.D. Thesis, Virginia Polytechnic Institute and State University, Blacksburg, Va., May 1974.

7. Newman, J. C. Jr., and Armen, Harry, Jr., "Elastic-Plastic Analysis of a Propagating Crack Under Cyclic Loading," AIAA paper No. 74-366, presented at the AIAA/ASME/SAE 15th Structures, Structural Dynamics, and Materials Conference, Las Vegas, Nev., 17-19 April 1974.

8. Newman, J. C., Jr., "A Finite-Element Analysis of Fatigue Crack Closure", Mechanics of Crack Growth. ASTM STP 590, American Society for Testing and Materials, 1976, pp. 281-301.

9. Ohji, K., Ogura, K., and Okubo, Y., "Cyclic Analysis of a Propagating Crack and its Correlation with Fatigue Crack Growth," Engineering Fracture Mechanics, 1975, Vol. 7, pp. 457-464.

10. Ogura, K. and Obji, K., "FEM Analysis of Crack Closure and Delay Effect in Fatigue Crack Growth Under Variable Amplitude Loading." Engineering Fracture Mechanics, 1977, Vol. 9, pp. 471-480.

11. Hutchinson, J. W., "Singular Behaviour at the End of a Tensile Crack in a Hardening Material". Journal of Mechanics and Physics of Solids, 1968, Vol. 16, pp. 13-31.

12. Rice, J. R. and Rosengren, G. F., "Plane Strain Deformation Near a Crack Tip in a Power Low Hardening Material," Journal of Mechanics and Physics of Solids, Vol. 16, 1968, pp. 1-12.

13. Atluri, S. N. and Nakagaki, M., "J-Integral Estimates for Strain-Hardening Materials in Ductine Fracture Problems," AIAA Journal, Vol. 15, No. 7, 1977. pp. 923-931.

14. Atluri, S. N. and Nakagaki, M. and Chen, W. H., "Fracture Analysis Under Large Scale Yielding: A Finite Deformation Embedded Singularity, Elastic-plastic Incremental Finite Element Solution". ASTM STP 631, American Society for Testing and Materials, 1977, pp. 43-61.

15. Atluri, S. N., "On Some New General and Complementary Energy Theorems for the Rate Problems in Finite Strain, Classical Elasto-Plasticity", Georgia Institute of Technology, Report GIT-ESM-SA-78-10, Aug. 1978. (In review for publication in J. Mechanics and Physics of Solids).

16. Atluri, S. N., "Complementary Energy Principles; Finite Strain Problems; and Finite Elements", presented at IUTAM symp. on Variational Methods in Engineering, Northwestern University, Sept. 11-13, 1978 (to appear in Proceedings to be published by Pergamon Press; S. Nemet-Nassar and K. Washizu, Editors).

17. Hofmeister, L. D., Greenbaum, G. A., and Evensen, D. A., "Large Strain, Elasto-Plastic Finite Element Analysis," AIAA Journal, Vol. 9, No. 7, pp. 1248-1254, 1971.

18. Chitaley, A. D. and Mclintock, F. A., "Elastic-plastic Mechanics of Steady Crack Growth under Anti-plane Shear". Journal of Mechanics and Physics of Solids", Vol. 19, 1971, pp. 147-163.

19. Rice, J. R., "Elastic-plastic Models for Stable Crack Growth," in Mechanics and Mechanisms of Crack Growth (Proc. Conf. at Cambridge, England, Apr. 1973), ed. M. J. May, British Steel Corporation Physical Metallurgy Center Publication, 1975, pp. 14-39.

20. Broberg, K. B., "On Stable Crack Growth," Journal of Mechanics and Physics of Solids, 1975, Vol. 23, pp. 215-237.

21. Prager, W., "A New Method of Analyzing Stress and Strains in Work-Hardening Plastic Solids," Journal of Applied Mechanics, Vol. 23, 1956, p. 493.

22. Ziegler, H., "A Modification of Prager's Hardening Rule,", Quart. Appl. Math., Vol. 17, No. 1, 1959 p. 55.

23. Bernard, P. J., Lindley, T. C., and Richards, C. E., "Mechanisms of Overload Retardation During Fatigue Crack Propagation", Fatigue Crack Growth Under Spectrum Loads, ASTM STP 595, American Society for Testing and Materials, 1976, pp. 78-97.

24. Bowie, O. L. and Neal, P. M., "A Note on the Central Crack in a Uniformally Stressed Strip", International Journal of Fracture Mechanics, Vol. 2, Nov. 1970, pp. 181-182.

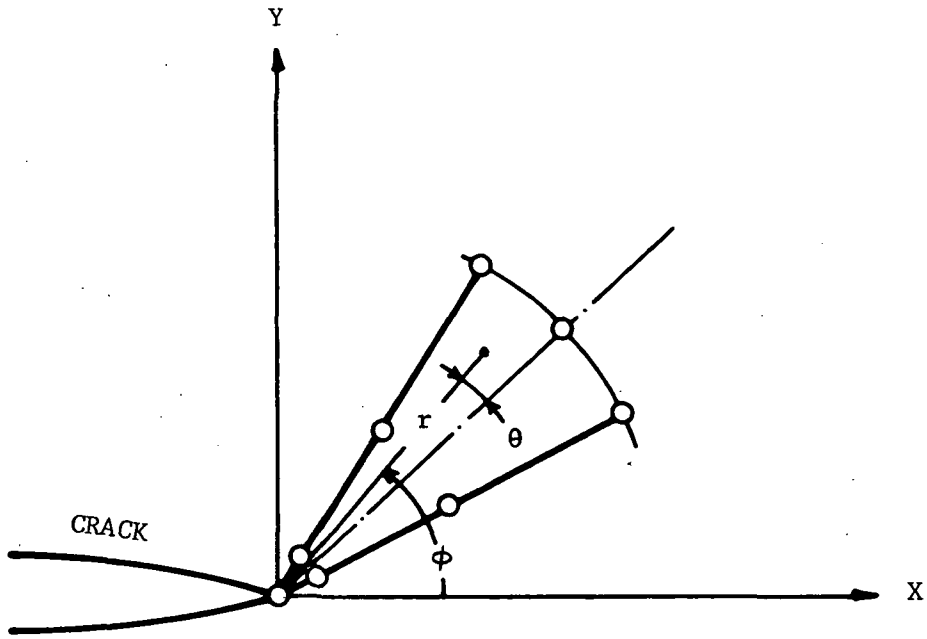

Fig. 1. Nomenclature for a Circular-Sector Shaped Singular Element.

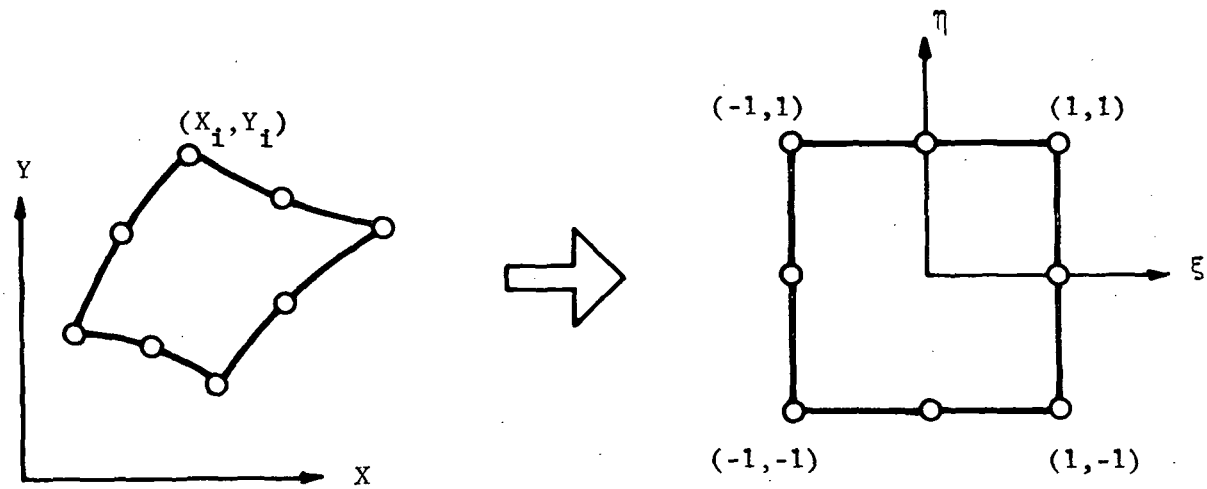

Fig. 2. 8-Noded Isoparametric "Regular" Element.

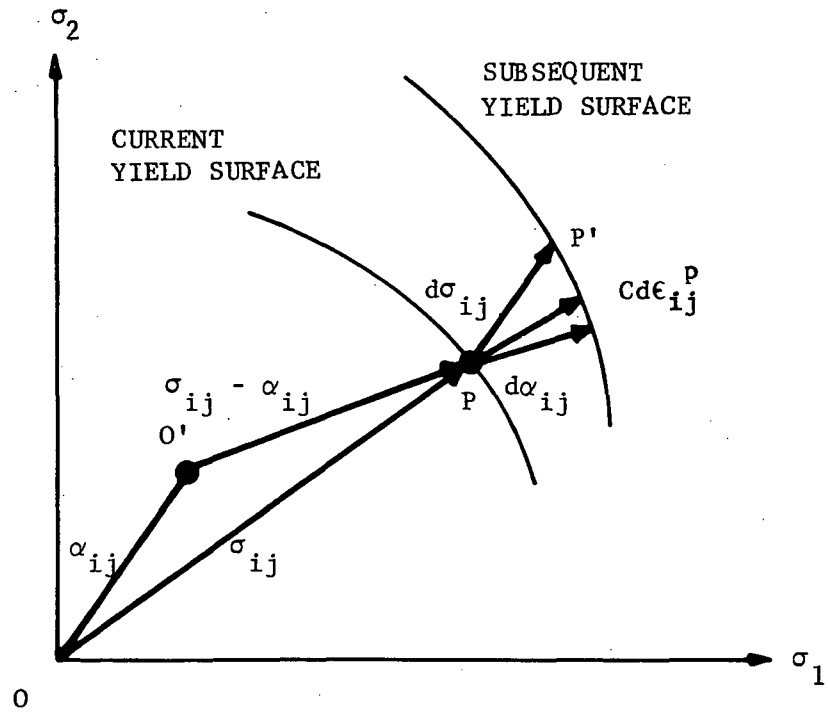

Fig. 3. Yield Surface Translation : Kinematic Hardening Law.

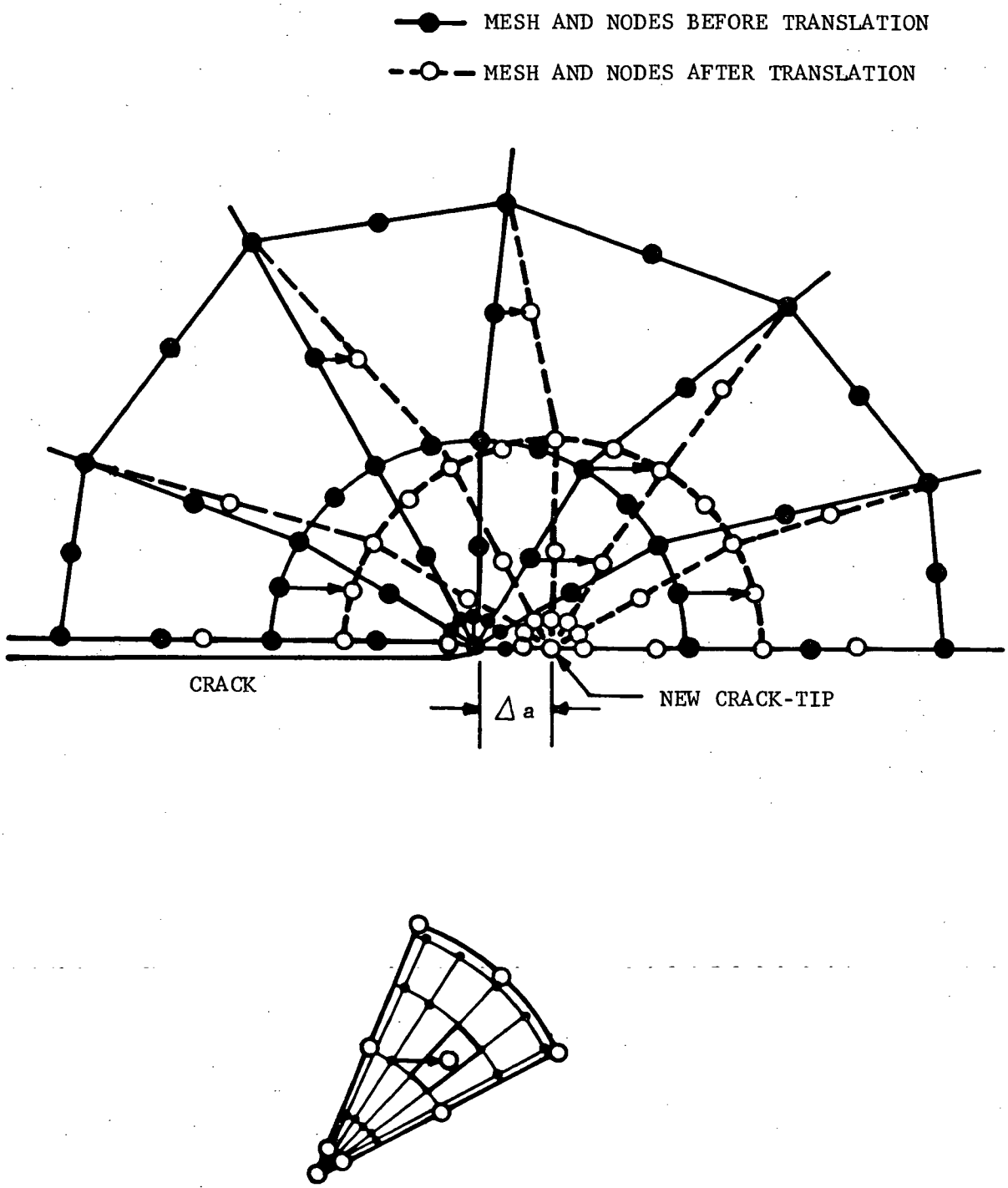

Fig. 4. Schematic Representation of Translation of Singular Elements.

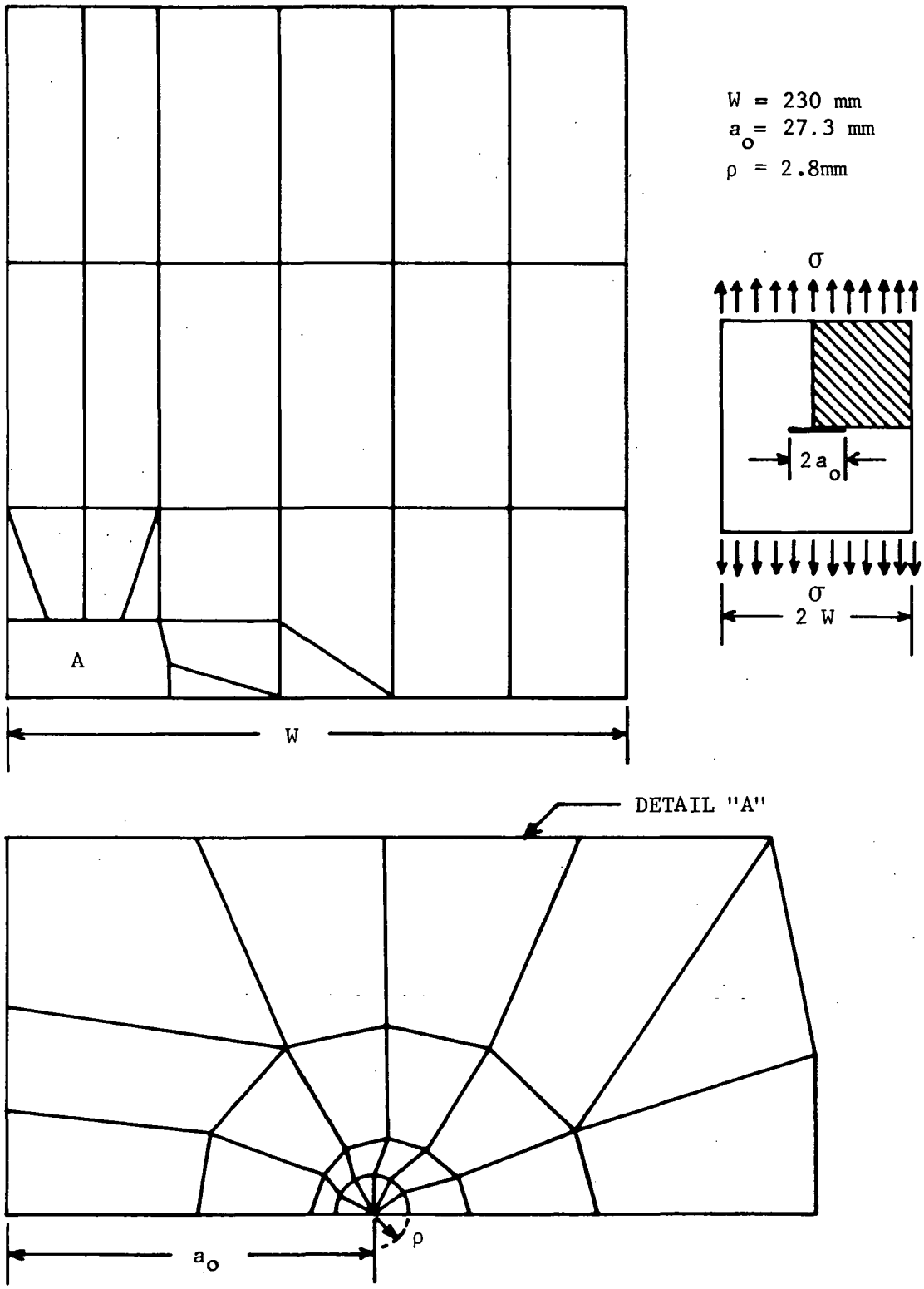

Fig. 5. Finite Element Model of a Center Cracked Specimen Under Uniaxial Cyclic Loading. (Singular Sector Elements Shown Within Detail "A")

PORTION OF DETAIL "A" IN FIG. 5

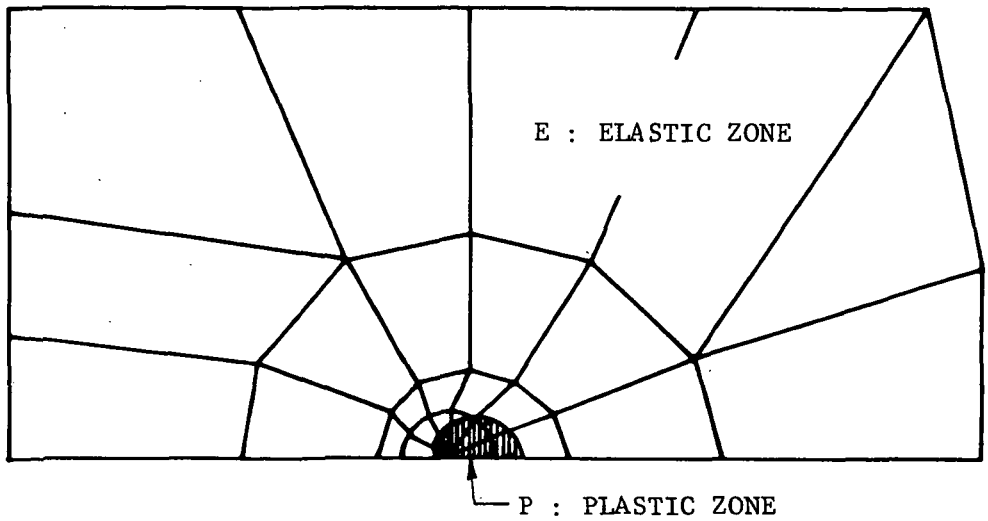

Fig. 6a. Representatve Size of Yield Zone at σ_{max}.

P : PLASTIC STIFFNESS MATRIX

E : ELASTIC STIFFNESS MATRIX

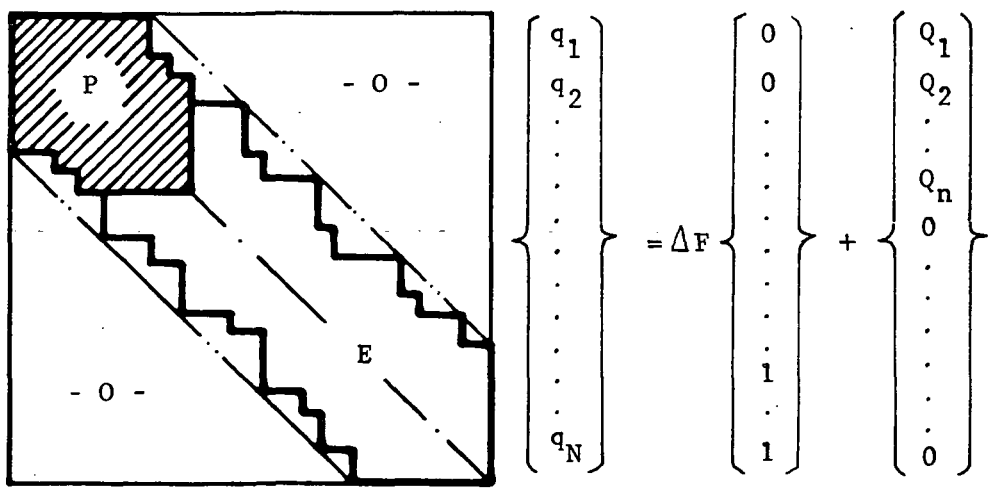

Fig. 6b. Schematic Representation of Incremental Equations in the Presence of Yielding.

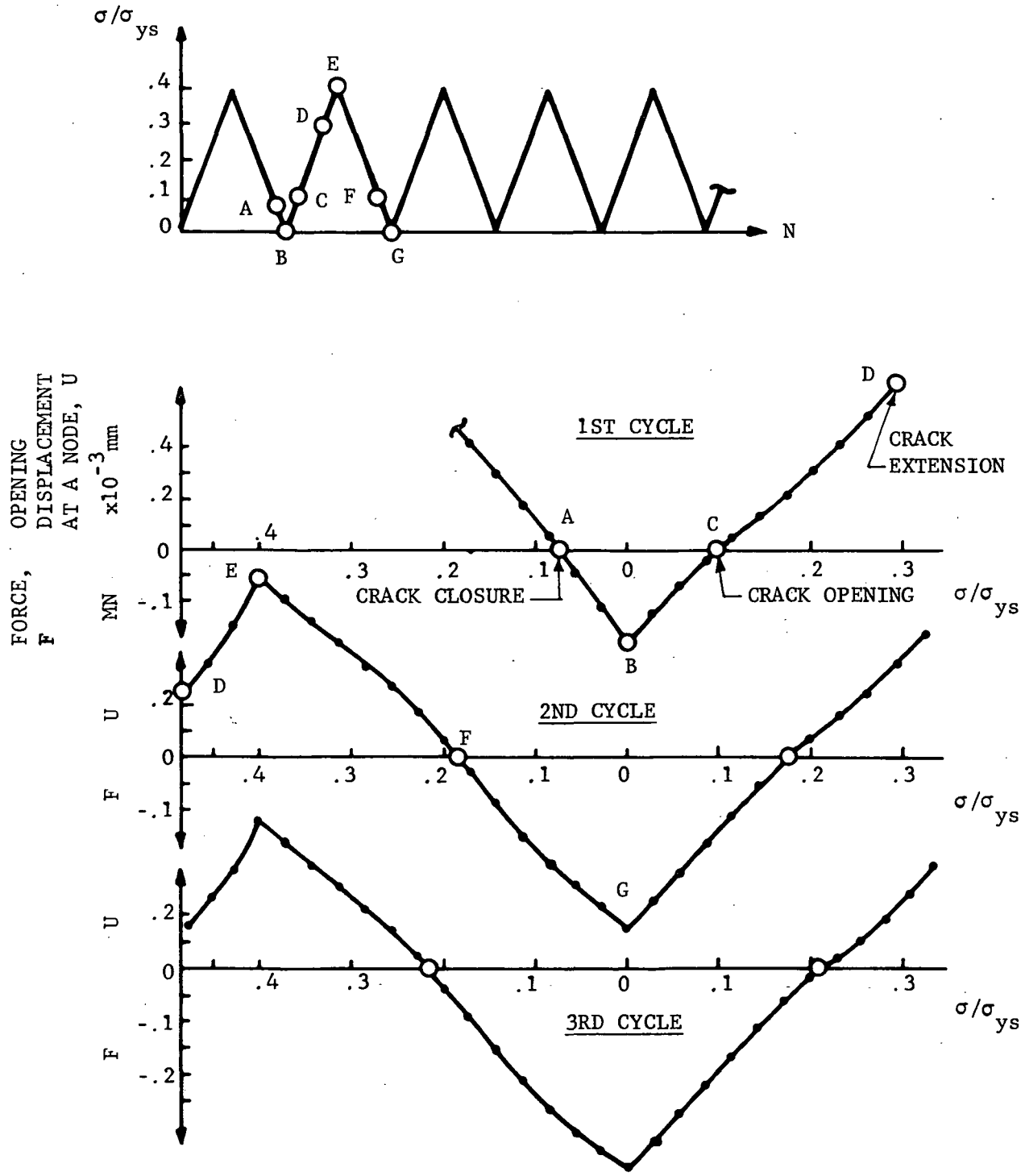

Fig. 7. Graphical Illustration of Procedures to find σ_{op} and σ_{cl} Through Extrapolation of COD and Crack-Tip Nodal Restraint Force.

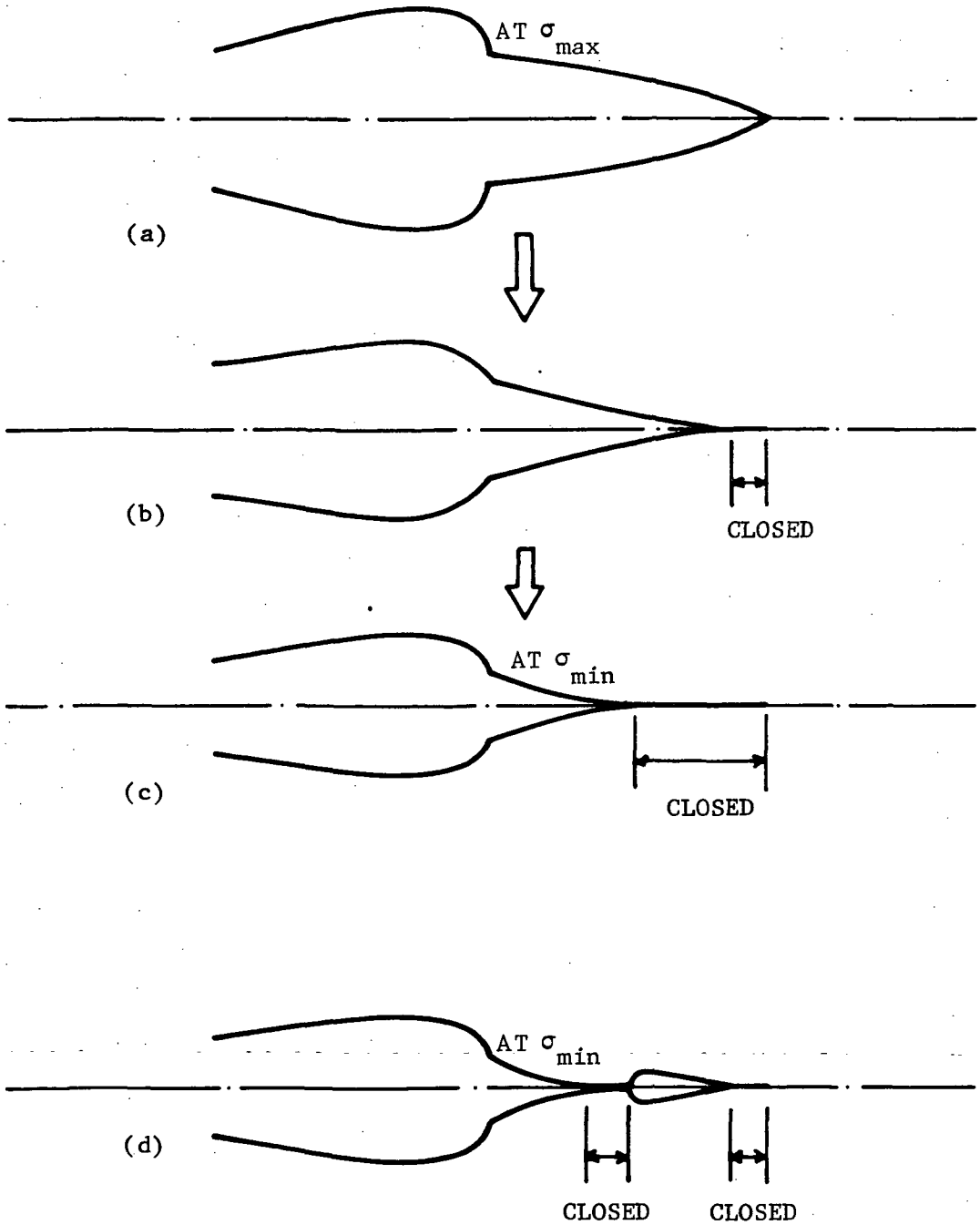

Fig. 8a - 8d. Representative Patterns of Crack Closure ; (8a - c) : Crack Closes Only at Nodes Closest to Crack-tip ; 8d : Crack Closure Occurs Also at Nodes Away From Crack-tip.

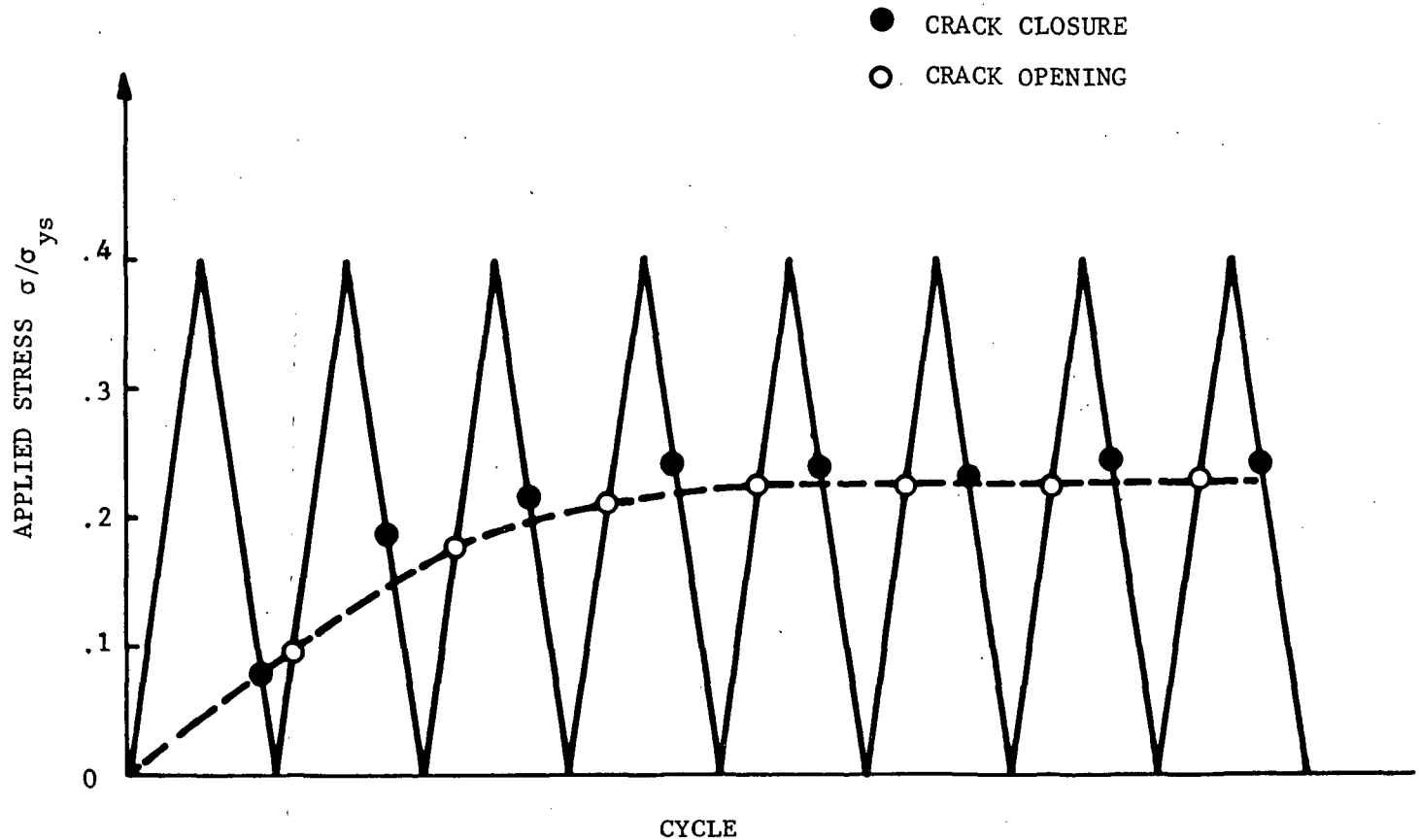

Fig. 9. Crack-Closure and Crack-Opening Stresses in Constant Amplitude (R=0) Cyclic Loading.

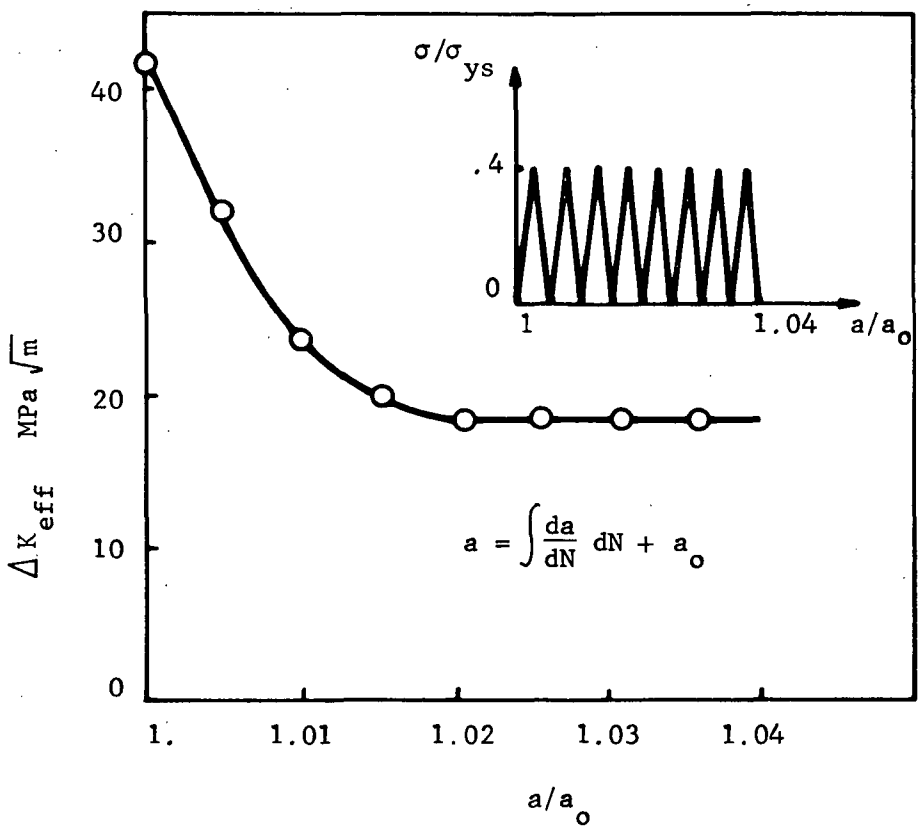

Fig. 10. ΔK_{eff} vs N Curve for Constant Amplitude Cyclic Loading.

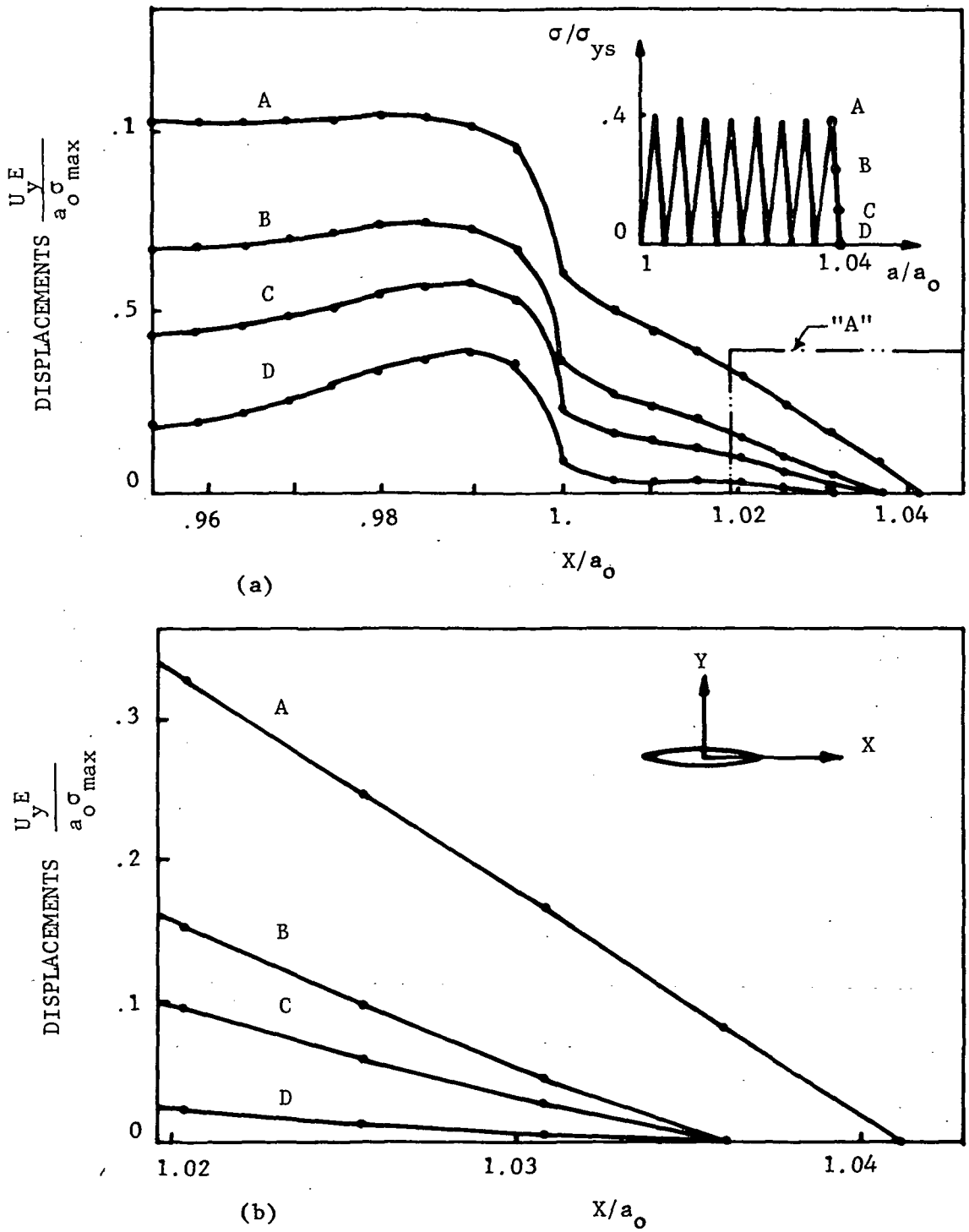

Fig. 11 ; 11a. Crack-Line Profile During Unloading in Constant Amplitude Loading ; 11b. Inset "A" in Fig. 11a. is magnified and Shown.

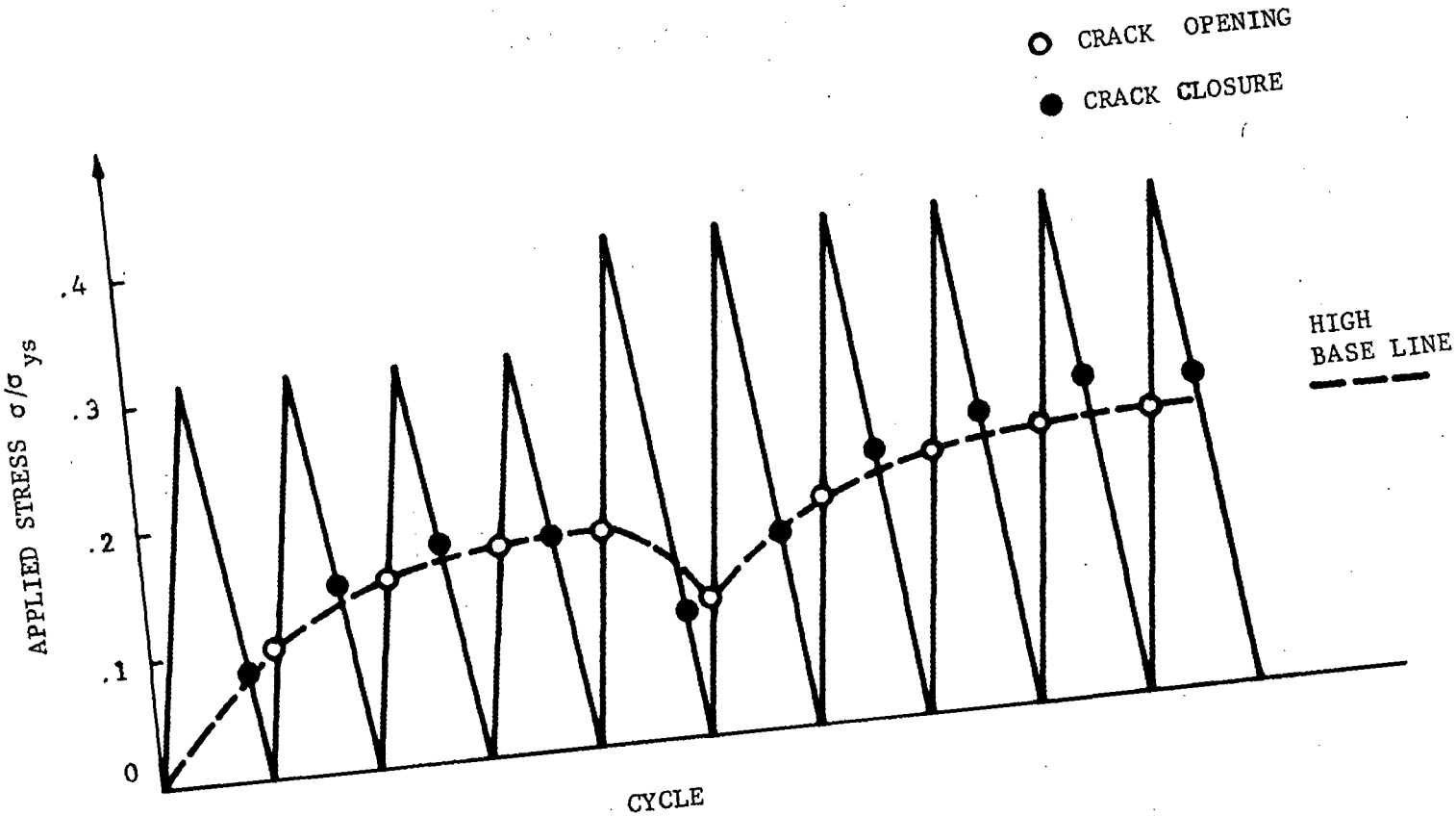

Fig. 12. Crack-Closure and Crack-Opening Stresses in Low-to-High Block Loading.

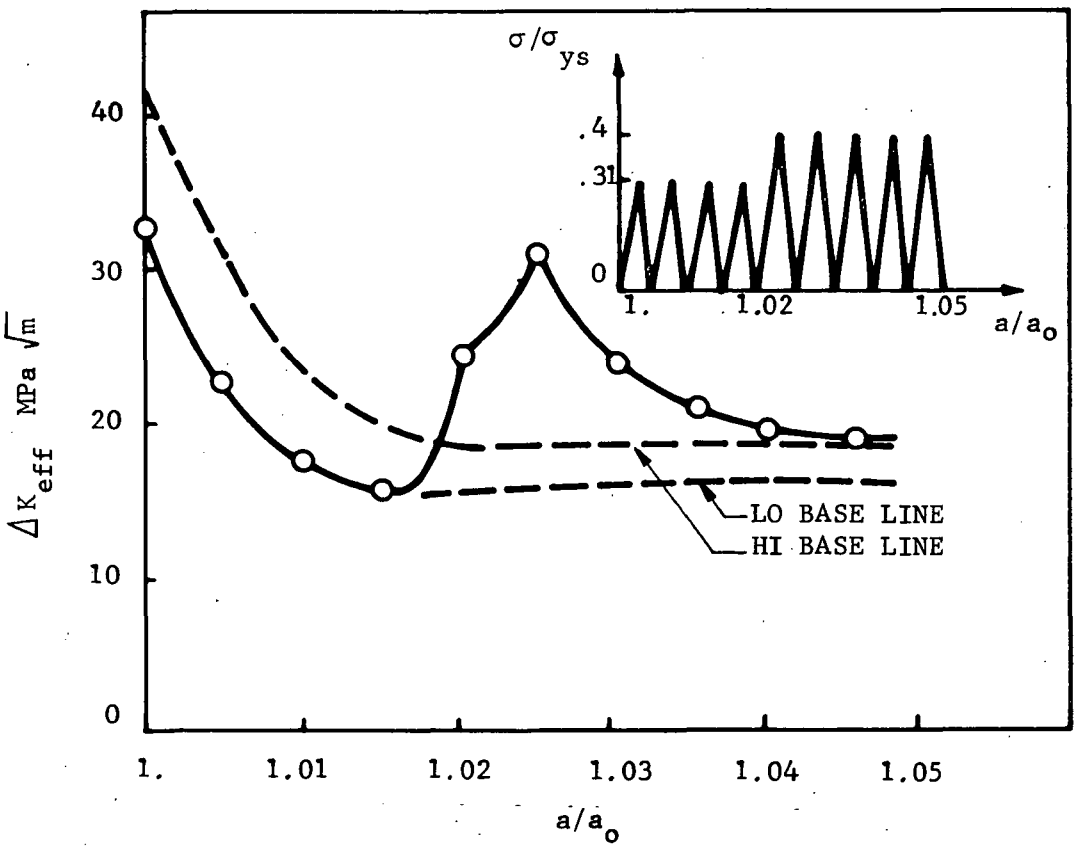

Fig. 13. ΔK_{eff} vs N Curve for Lo-To-High Block Loading.

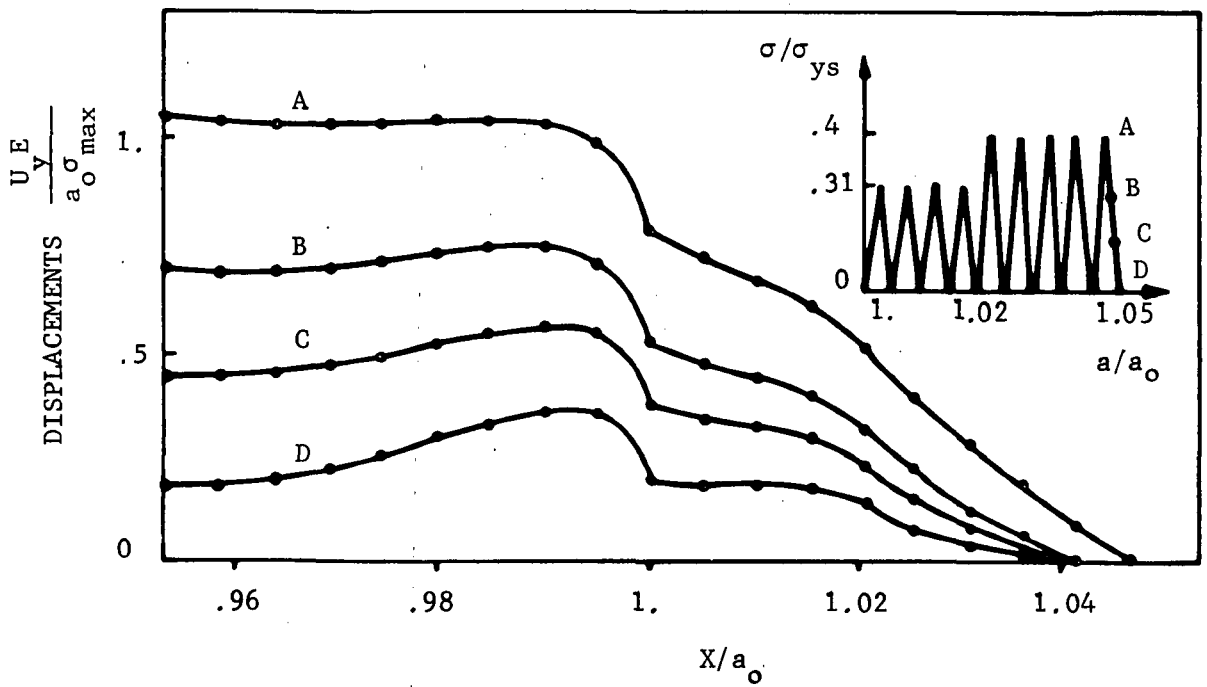

Fig. 14. Crack-Line Profile During Unloading in Low-To-High Block Loading.

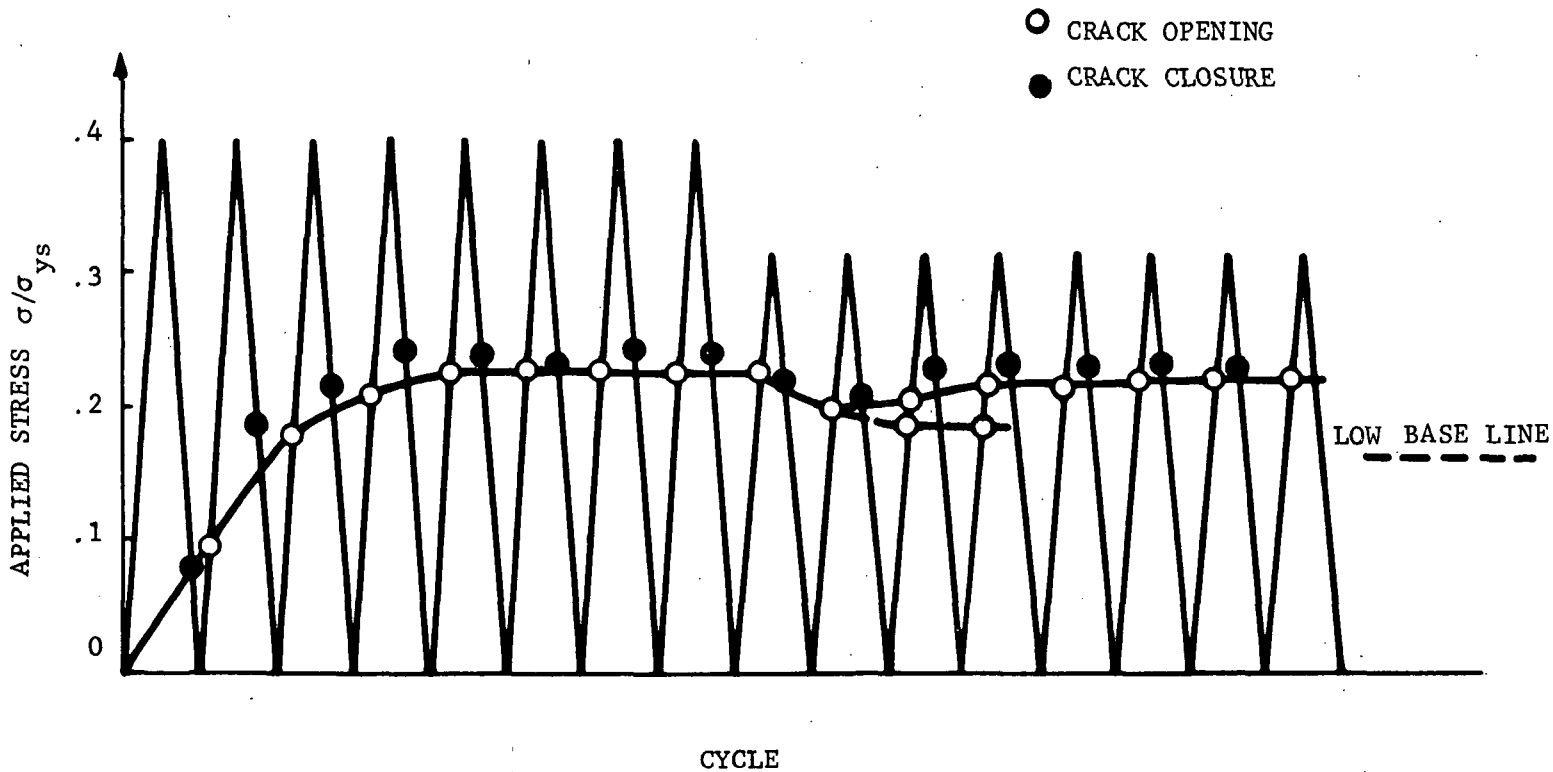

Fig. 15. Crack-Closure and Crack-Opening Stresses in High-to-Low Block Loading.

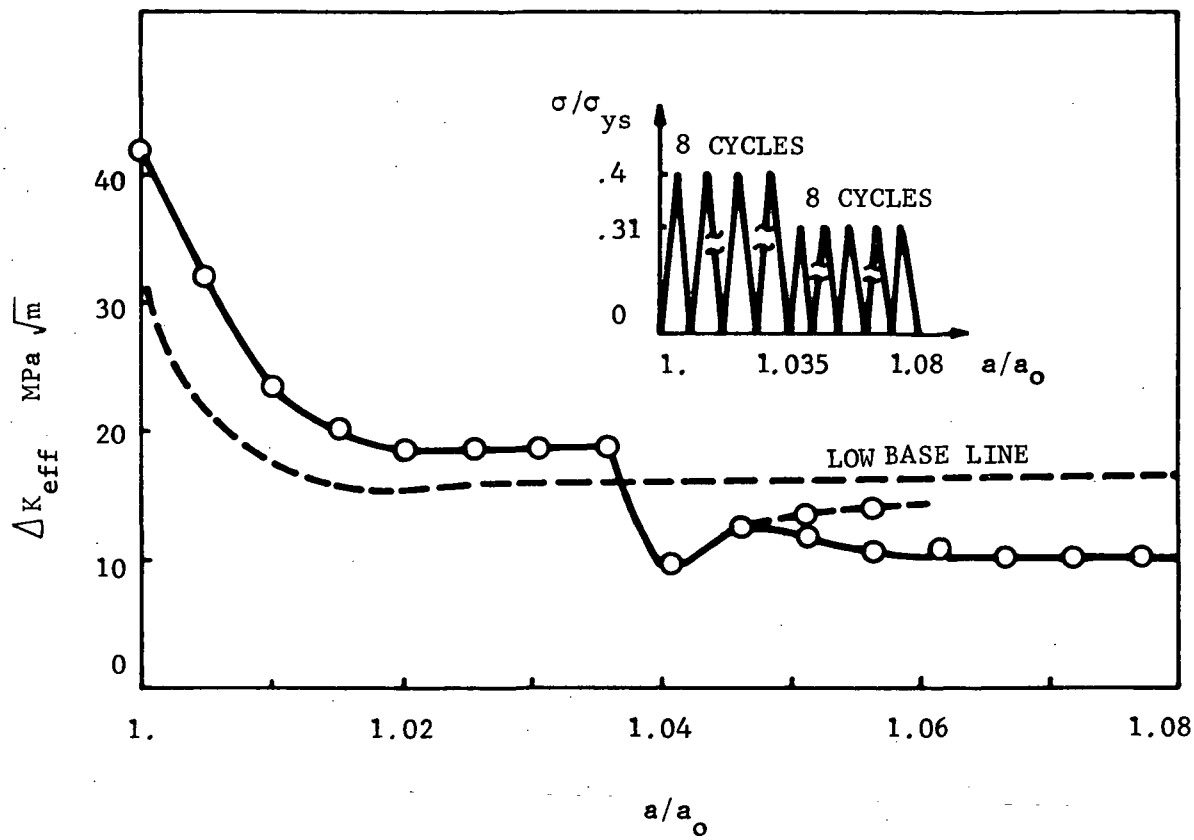

Fig. 16. ΔK_{eff} vs N Curve for High-to-Low Block Loading.

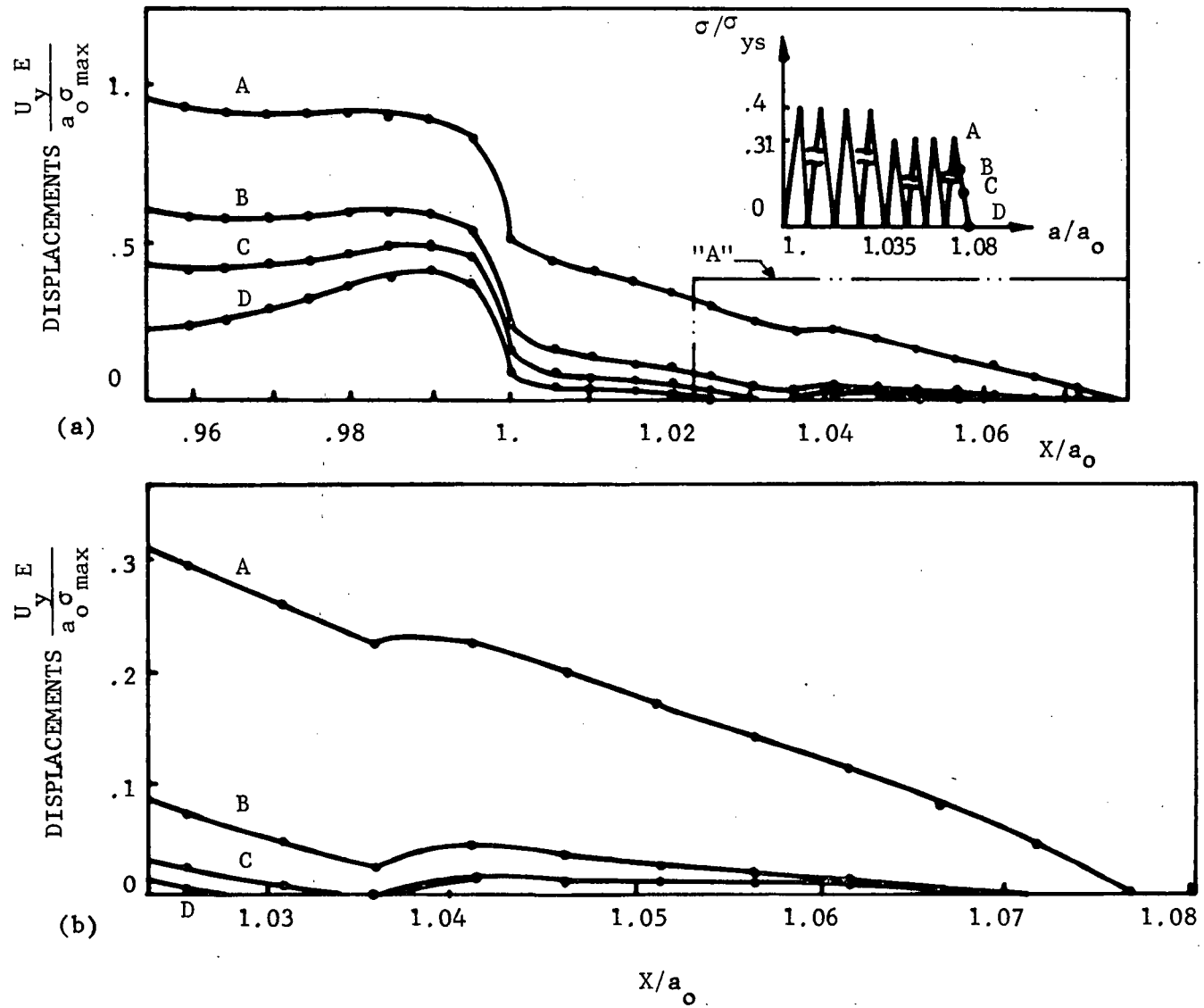

Fig. 17 ; 17a : Crack-Line Profile During Unloading in High-to-Low Block Loading :
17b : Inset "A" in Fig. 17a. is Magnified and Shown.

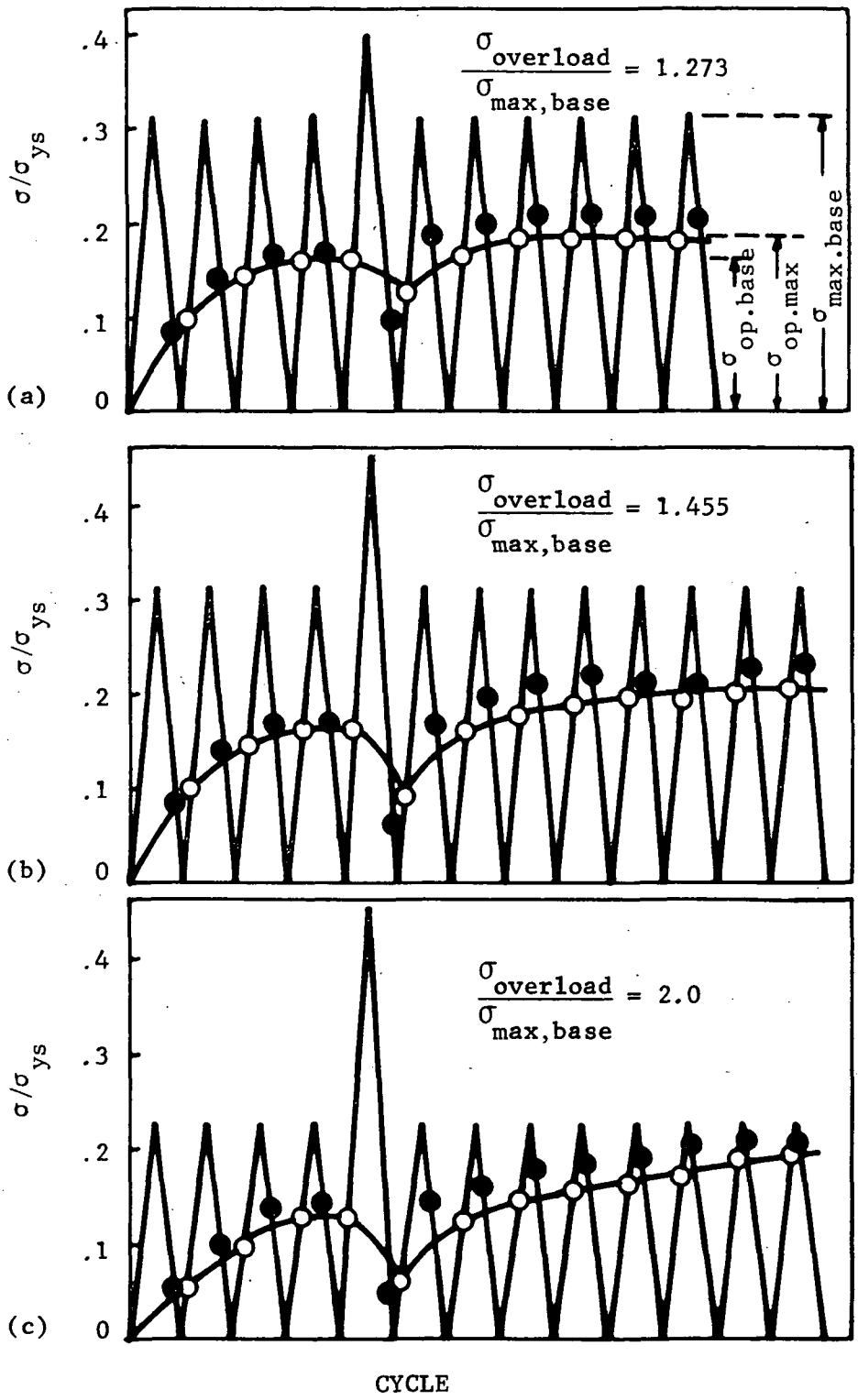

Fig. 18a - c : Crack-Closure and Crack-Opening Stress for Three Different Cases of a Single Over-Load.

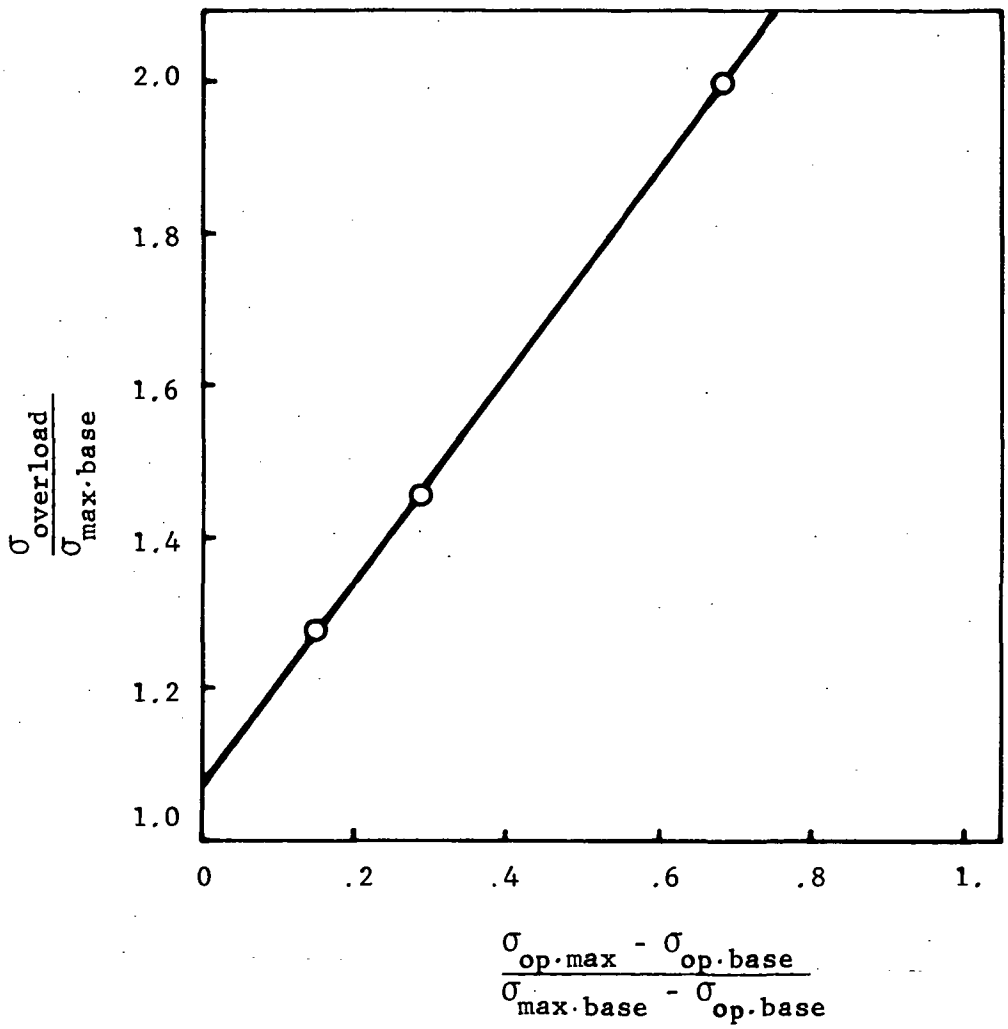

Fig. 19. Effect of Overload-Stress Ratio on $\frac{\sigma_{op\cdot max} - \sigma_{op\cdot base}}{\sigma_{max\cdot base} - \sigma_{op\cdot base}}$

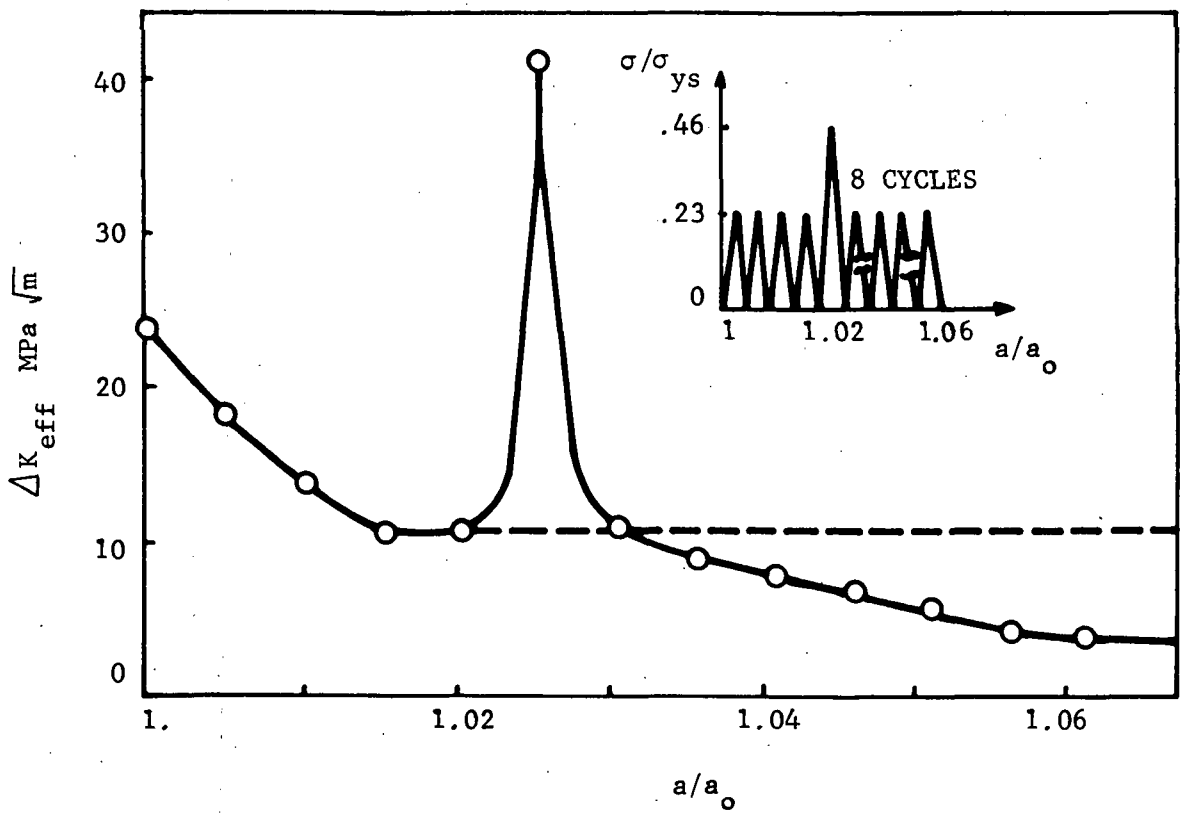

Fig. 20. ΔK_{eff} vs N Curve for Single Over-Load Case.

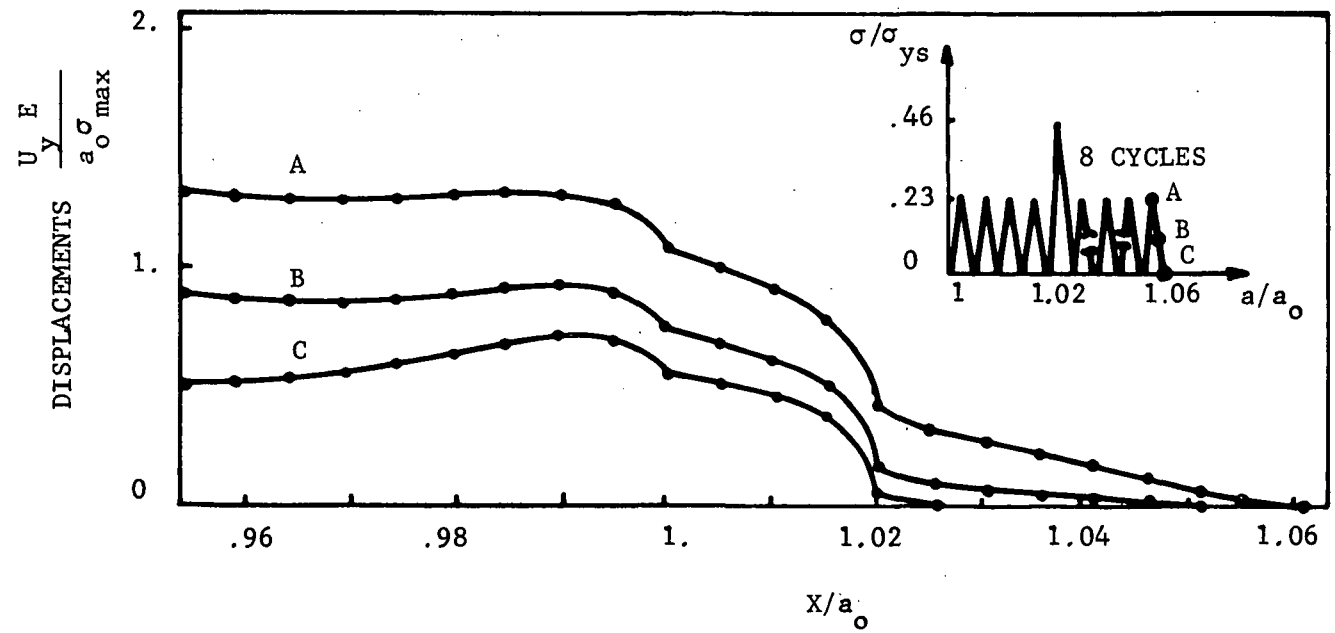

Fig. 21. Crack-Line Profile During Unloading After a Single Over-Load.

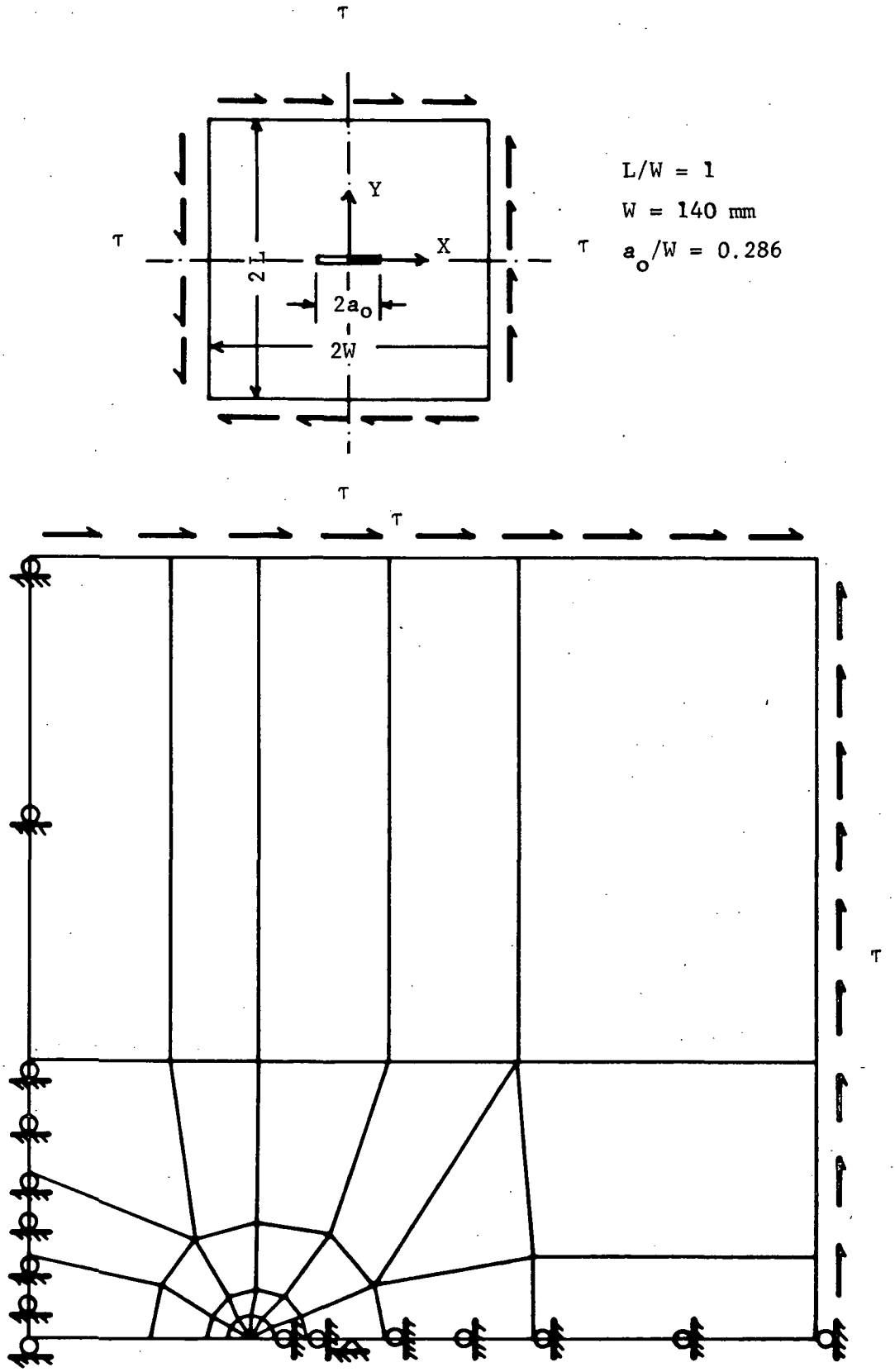

Fig. 22. Geometry and Finite Element Model of a Center-Cracked Panel Under Pure Shear Cyclic Loading.

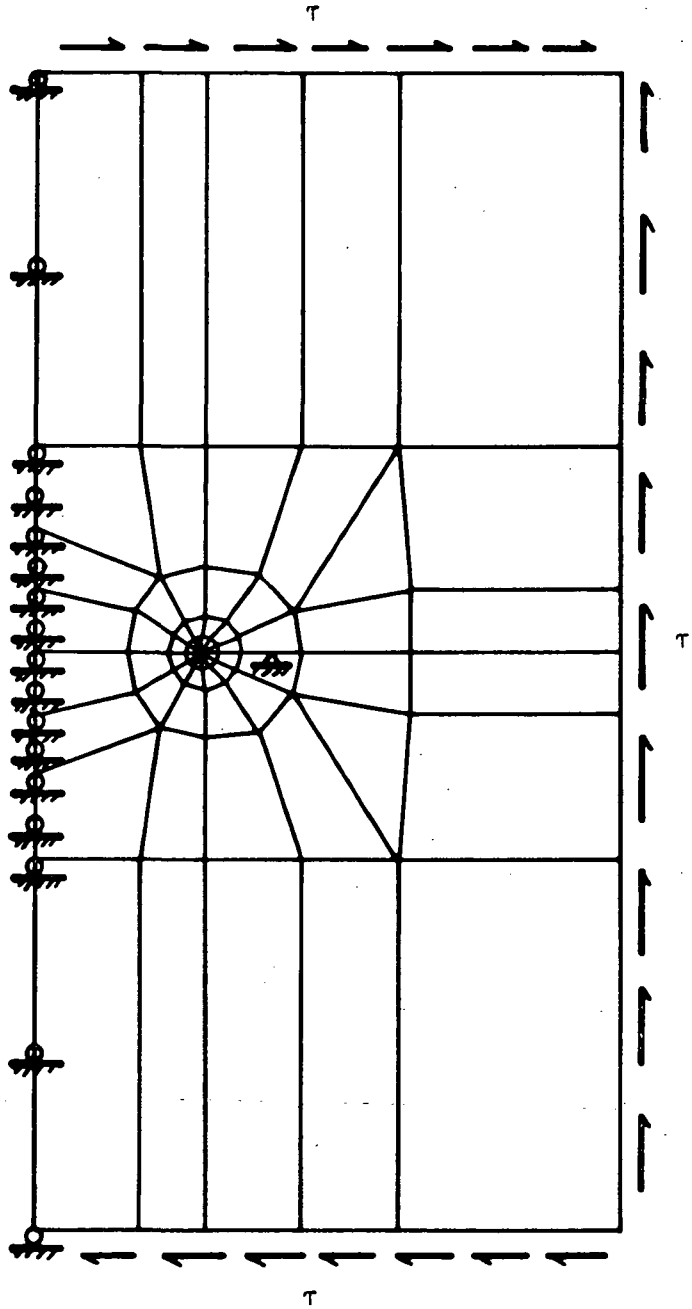

Fig. 23. An Alternate Finite Element Model of a Center-Cracked Panel Under Pure Shear Cyclic Loading.

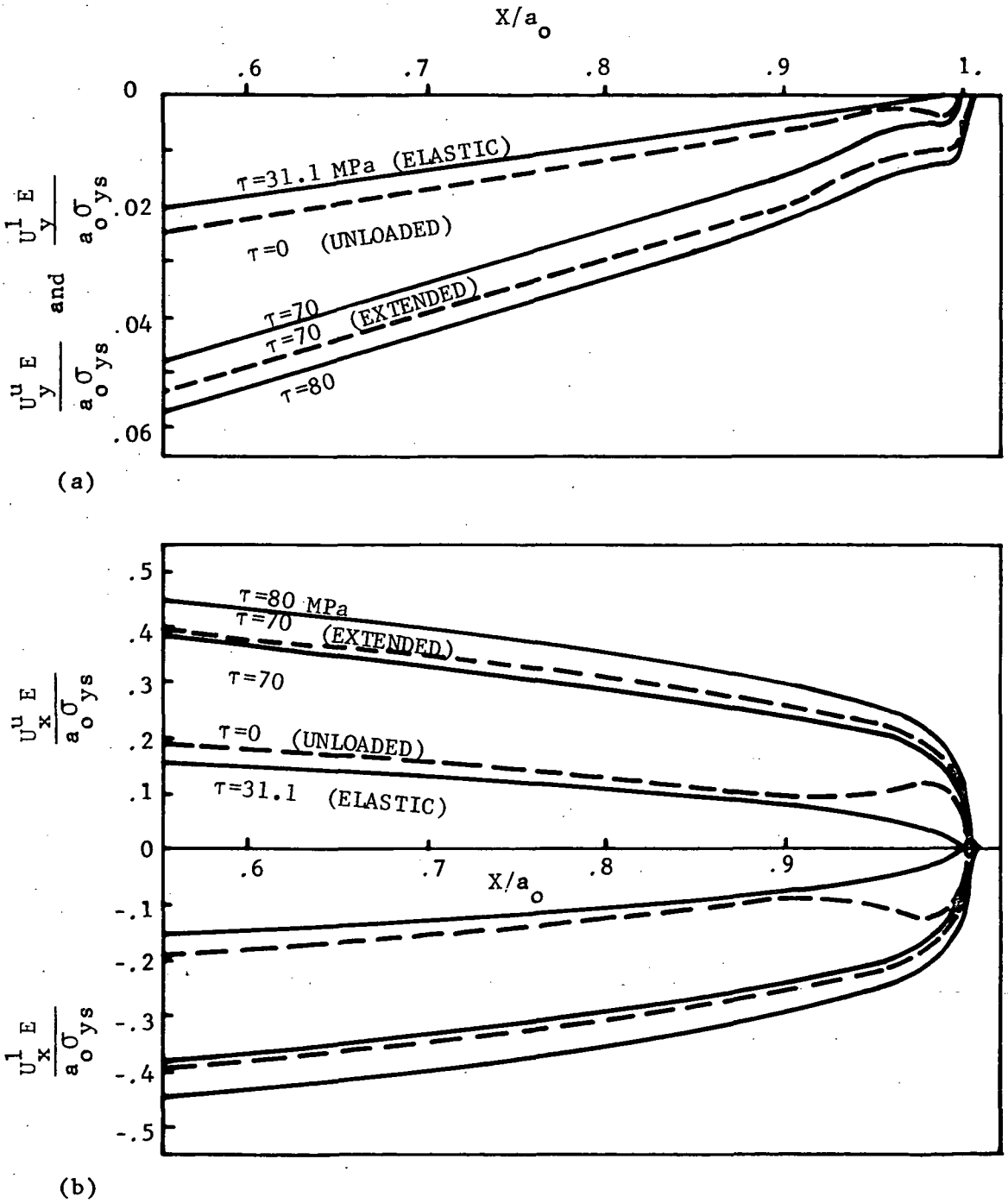

Fig. 24 ; 24a : Normal Displacement Profiles of the Upper and Lower Surfaces of the Crack ; 24b : Tangential Displacement Profiles of Upper and Lower Surfaces of the Crack.

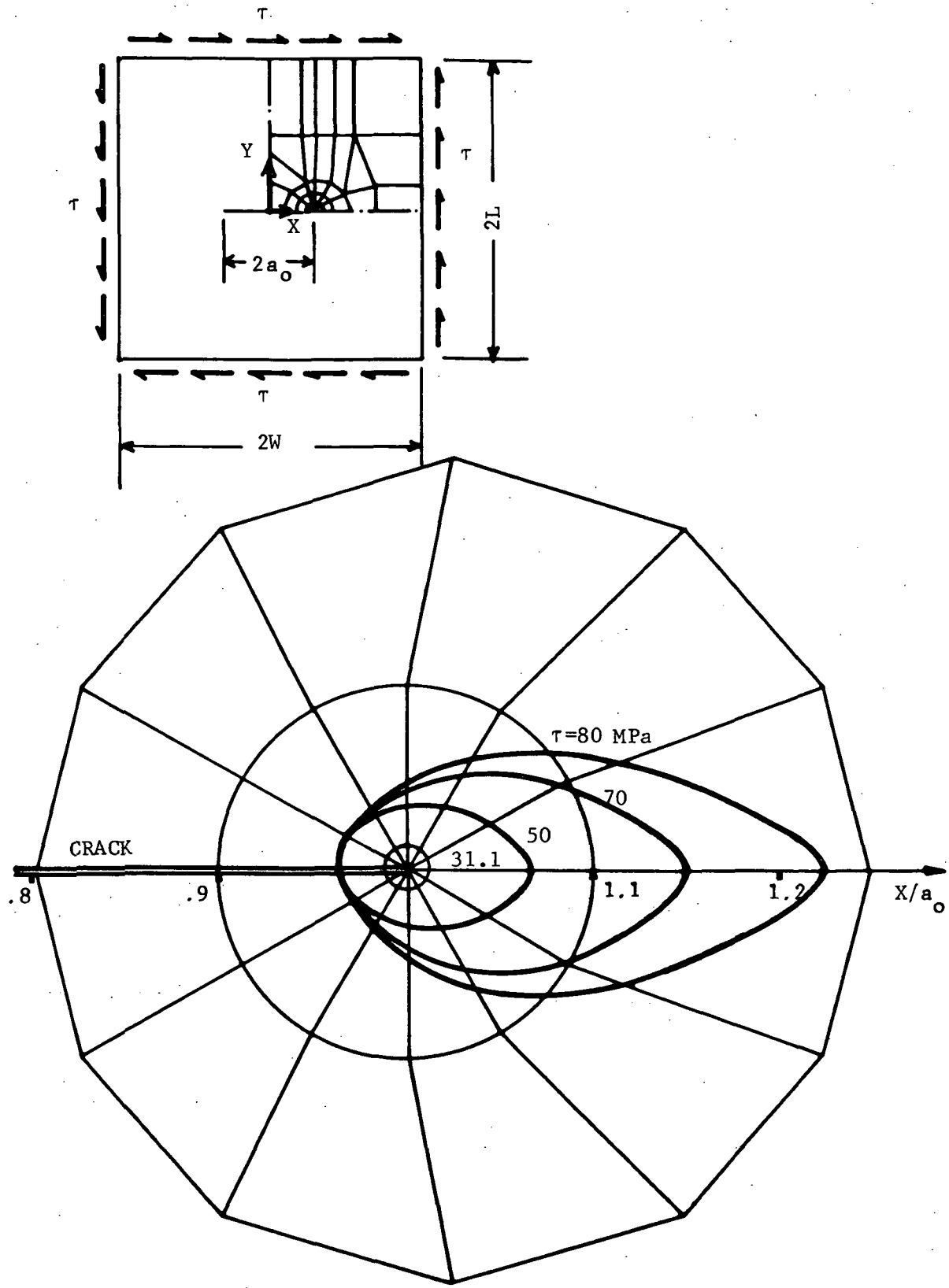

Fig. 25. Plastic-Zone Near Crack-Tip in a Center-Cracked Panel Under Pure Shear Cyclic Loading.

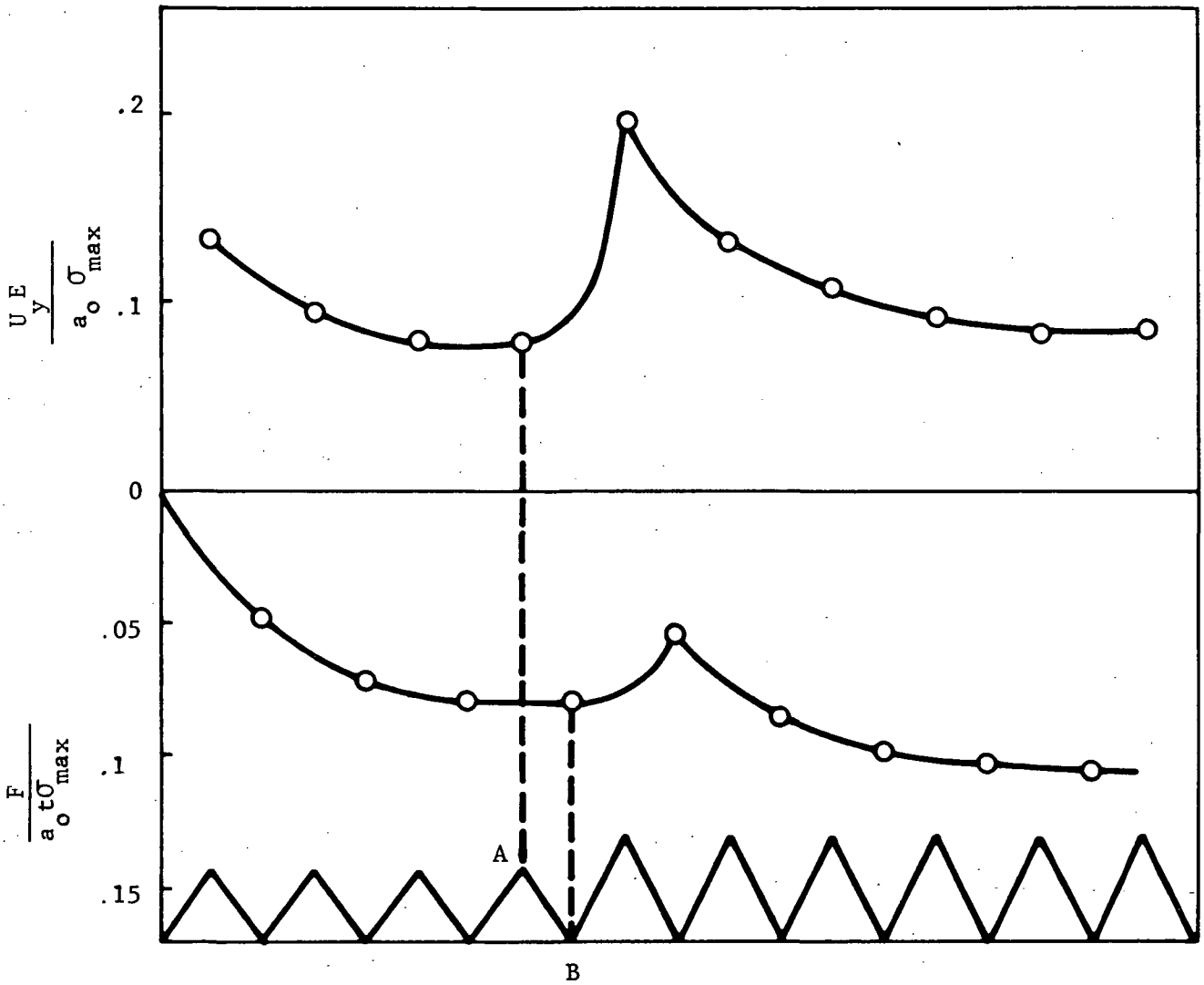

Fig. 26. Maximum Opening Displacement at a Node Closest to Crack-Tip and Total Compressive Force over Closed Area Near Crack-Tip in Each Cycle, in Low-to-High Block Loading.

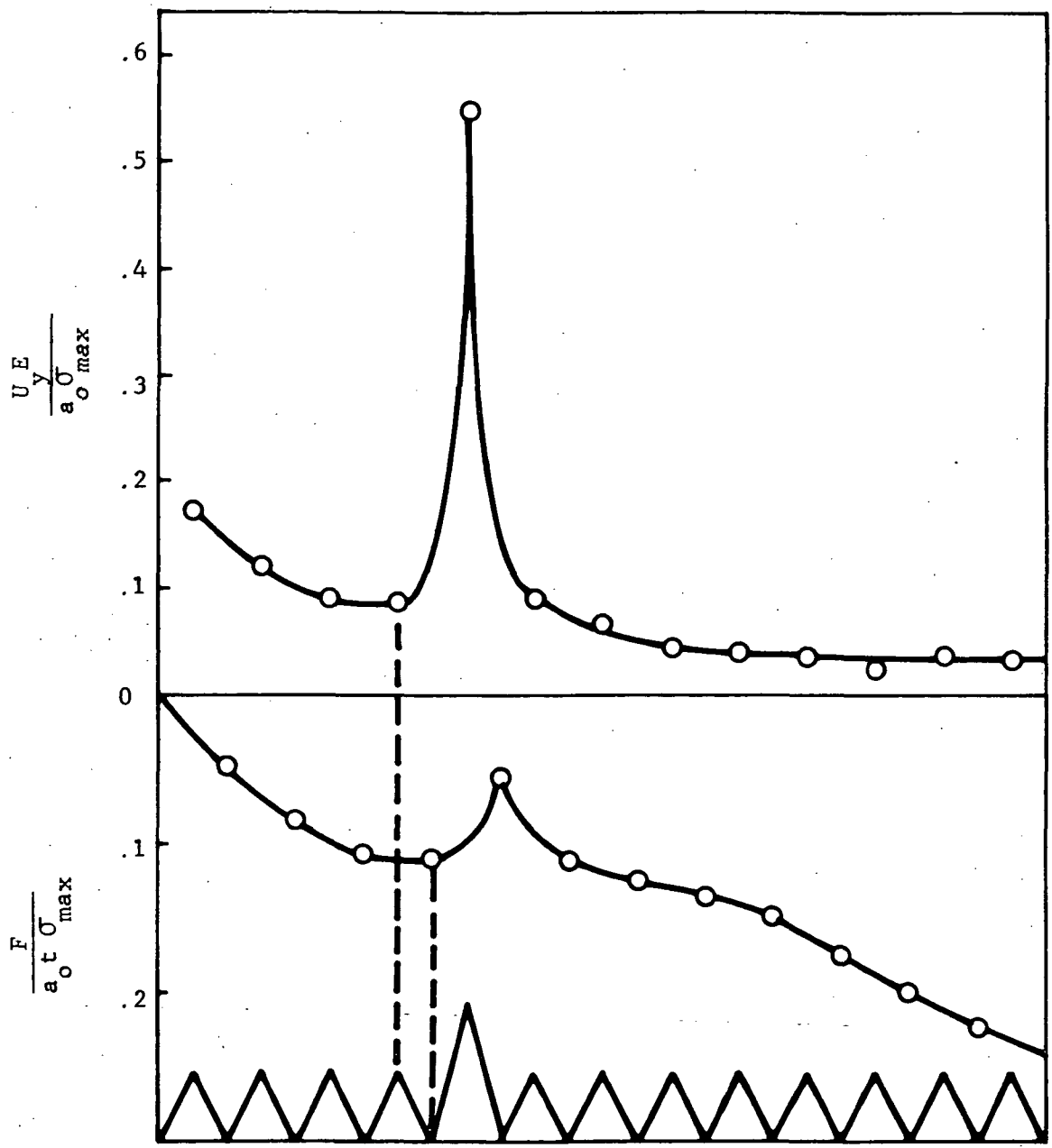

Fig. 27. Maximum Opening Displacement at a Node Closest to Crack-Tip and Total Compressive Force over Closed Area Near Crack-Tip in Each Cycle, in a Single Over-Load Case.